BROAD Hβ EMISSION-LINE VARIABILITY IN A SAMPLE OF 102 LOCAL ACTIVE GALAXIES

Jordan N. Runco[1], Maren Cosens[1], Vardha N. Bennert[1], Bryan Scott[1], S. Komossa[2], Matthew A. Malkan[3],
Mariana S. Lazarova[4], Matthew W. Auger[5], Tommaso Treu[3], and Daeseong Park[6]

[1] Physics Department, California Polytechnic State University, San Luis Obispo CA 93407, USA; jrunco@calpoly.edu, mcosens@calpoly.edu, vbennert@calpoly.edu
[2] Max-Planck-Institut für Radioastronomie, Auf dem Hügel 69, D-53121, Bonn, Germany
[3] Department of Physics, University of California, Los Angeles, CA 90095, USA; malkan@astro.ucla.edu, tt@physics.ucsb.edu
[4] Department of Physics and Physical Science, University of Nebraska Kearney, Kearney, NE 68849, USA; lazarovam2@unk.edu
[5] Institute of Astronomy, Madingley Road, Cambridge CB3 0HA, UK; mauger@ast.cam.ac.uk
[6] Korea Astronomy and Space Science Institute, Daejeon, 34055, Korea; daeseongpark@kasi.re.kr

ABSTRACT

A sample of 102 local ($0.02 \leqslant z \leqslant 0.1$) Seyfert galaxies with black hole masses $M_{BH} > 10^7 M_\odot$ was selected from the Sloan Digital Sky Survey (SDSS) and observed using the Keck 10 m telescope to study the scaling relations between M_{BH} and host galaxy properties. We study profile changes of the broad Hβ emission line within the three to nine year time frame between the two sets of spectra. The variability of the broad Hβ emission line is of particular interest, not only because it is used to estimate M_{BH}, but also because its strength and width are used to classify Seyfert galaxies into different types. At least some form of broad-line variability (in either width or flux) is observed in the majority (∼66%) of the objects, resulting in a Seyfert-type change for ∼38% of the objects, likely driven by variable accretion and/or obscuration. The broad Hβ line virtually disappears in 3/102 (∼3%) extreme cases. We discuss potential causes for these changing look active galactic nuclei. While similar dramatic transitions have previously been reported in the literature, either on a case-by-case basis or in larger samples focusing on quasars at higher redshifts, our study provides statistical information on the frequency of Hβ line variability in a sample of low-redshift Seyfert galaxies.

Key words: accretion, accretion disks – galaxies: active – galaxies: evolution – galaxies: Seyfert – galaxies: statistics

1. INTRODUCTION

Observed relations between the mass of the supermassive black hole (M_{BH}) at the center of a galaxy and the properties of its host galaxy—such as host galaxy mass (Magorrian et al. 1998), luminosity (Kormendy & Richstone 1995), and stellar velocity dispersion (Ferrarese & Merrit 2000; Gebhardt et al. 2000)—imply a relationship between galaxy evolution and black hole (BH) growth (for a recent review see Kormendy & Ho 2013; Graham 2016, and references therein). In the local universe, M_{BH} can be measured by spatially resolving the BH sphere of influence using stellar or gas kinematics (e.g., van der Marel et al. 1998; Gebhardt et al. 2000). At larger distances the only way to estimate M_{BH} is by resolving the BH sphere of influence as it responds to variations in continuum in galaxies with an active galactic nucleus (AGN). In AGNs, the BH is actively growing via an accretion disk of in-falling material. The high-energy photons emitted by the hot accretion disk ionize the surrounding gas clouds, the broad-line region (BLR) in the vicinity of the BH, and the narrow-line region (NLR) further out. Reverberation mapping (Wandel et al. 1999; Kaspi et al. 2005; Bentz et al. 2013) traces variations in the accretion disk continuum luminosity and the time-delayed response of the BLR flux to determine the size of the BLR, using light-travel time arguments. The velocity of the BLR gas can be determined from the Doppler broadening of the emission lines (such as the broad Hβ line in the rest-frame optical). By assuming a dimensionless virial coefficient to describe the kinematics and geometry of the BLR, the velocity and size of the BLR combined yield M_{BH}. More recently, there have been attempts to estimate M_{BH} in individual objects independent of a virial coefficient by modeling reverberation-mapped data directly and constraining the geometry and kinematics of the BLR (see e.g., Pancoast et al. 2014, and references therein).

Seyfert galaxies are low-luminosity AGNs for which the host galaxy can be easily resolved, thus making them attractive targets for the study of the M_{BH} scaling relations. In fact, for a few Seyfert galaxies, M_{BH} estimates from both dynamical AO measurements as well as reverberation mapping are available (Hicks & Malkan 2008). Seyfert galaxies are categorized into different types based on their emission line profiles, ranging from type-1 to type-2 with subclasses (type-1.5, 1.8, and 1.9) in between. Type-1 Seyferts display both broad and narrow components of emission lines, while type-2 Seyferts show only the narrow components. The intermediate Seyfert types show varying levels of broad component emission. The Balmer series in the optical regime is generally used to classify Seyfert type (Osterbrock & Koski 1976; Osterbrock 1977, 1981). Table 1 summarizes the different Seyfert-type classifications).

In the framework of the so-called standard unified model for active galaxies, all Seyfert galaxies are thought to be intrinsically the same but viewed from a different angle. The key to this model is a region of cold gas and dust called the dusty torus which surrounds the BLR. If seen edge on, the dusty torus can shield both the accretion disk continuum and the broad emission lines from the observer's view, resulting in a type-2 Seyfert galaxy. If seen face on, however, both accretion disk and BLR are visible, resulting in a type-1 Seyfert galaxy. Intermediate types-1.5, 1.8, and 1.9 are viewed along the edges of the dusty torus where it is not optically thick enough to fully block the broad lines. In other words, in this simplified model the presence or absence of broad lines is attributed solely to viewing orientation, meaning that the Seyfert type of a galaxy does not change. (Note that the

Table 1
Seyfert-type Classifications

Type (1)	Description (2)
Type-1	Both broad and narrow components in all Balmer lines.
Type-1.5	Broad and narrow components can be identified in Hα and Hβ. Broad component of higher-order Balmer lines are weakening.
Type-1.8	Broad Hβ is weak but detectable. No higher-order Balmer lines have a broad component.
Type-1.9	Shows broad Hα but no higher-order Balmer lines have a broad component.
Type-2	No broad emission lines.

Note. Column (1): Seyfert-type. Column (2): Seyfert type classification based on the strength of the Hβ and Hα lines (Osterbrock 1977, 1981).

orientation of the torus is entirely independent of the host galaxy orientation.)

However, in the literature there have been many reports of apparent Seyfert-type changes (e.g., Tohline & Osterbrock 1976; Kollatschny & Fricke 1985; Storchi-Bergmann et al. 1993; Aretxaga et al. 1999; Eracleous & Halpern 2001; Trippe et al. 2008; Denney et al. 2014; Shappee et al. 2014; Parker et al. 2015). These changes can occur in either direction. NGC 4151 is one of the most notable and cited examples. Originally classified as a type-1.5 (Osterbrock 1977), the broad emission lines disappeared throughout the 1980s (Antonucci & Cohen 1983; Lyutyi et al. 1984; Penston & Perez 1984) but have since returned (Shapovalova et al. 2010). Another well-studied example is Mrk 590, which has been observed over a 40 year timescale. First observed as a type-1.5, Mrk 590 transitioned to a type-1 before the broad lines disappeared, making it a type ~1.9–2 Seyfert (Denney et al. 2014). Possible causes of these changing look AGNs include changes in extinction (due to our line of sight grazing the dusty torus, for instance; e.g., Goodrich 1989; Leighly et al. 2015), or changes in the AGN accretion rate (e.g., Nicastro 2000; Korista & Goad 2004; Elitzur et al. 2014) In rare cases, the increase in accretion rate could be due to the tidal disruption and accretion of a star, and a few cases of dramatic broad-line variability possibly linked to this scenario have been reported in recent years (e.g., Komossa et al. 2008; Arcavi et al. 2014; LaMassa et al. 2015; Merloni et al. 2015).

A certain degree of variability in the flux and profile of the BLR emission as a response to changes in the continuum flux (and thus accretion) is not only expected, but in fact forms the basis for reverberation mapping studies. Such studies have shown that variations in continuum flux and that of the broad Balmer lines are correlated in a way so that the derived M_{BH} does not change (Bentz et al. 2007; Park et al. 2012; Barth et al. 2015). However, extreme variability leading to a type change seems to be rare.

Here we address the question of the frequency of these changing look AGNs by taking advantage of a statistical sample of 102 local Seyfert galaxies with archival spectra from the Sloan Digital Sky Survey (SDSS) and high-quality Keck spectra taken 6.4 ± 1.8 years apart. The paper is organized in the following manner. Section 2 summarizes the sample selection, observations, and data reduction. Section 3 describes the analysis of the data. Section 4 discusses the derived quantities and results from the data. Section 5 concludes with a summary. Throughout the paper a Hubble constant of $H_o = 70 \, \mathrm{km \, s^{-1}}$, $\Omega_\lambda = 0.7$, and $\Omega_M = 0.3$ is assumed.

2. SAMPLE SELECTION, OBSERVATIONS, AND DATA REDUCTION

The primary goal behind sample selection and observations is the creation of a local baseline for the BH mass scaling relations of active galaxies presented by Bennert et al. (2011, 2015) and Harris et al. (2012), whose papers describe the sample selection, the Keck observations, and the Keck data reduction in detail. Here we provide only a brief summary.

2.1. Sample Selection

A sample of 102 local ($0.02 \leqslant z \leqslant 0.1$) type-1 Seyfert galaxies was selected from the SDSS data release six (DR6) (Adelman-McCarthy et al. 2008). Objects were selected on the basis of a broad Hβ emission line with an estimated $M_{BH} > 10^7 M_\odot$ (Bennert et al. 2011; Harris et al. 2012). Note that of these 102 objects, only 79 are used by Bennert et al. (2015) to study the M_{BH}–σ relation because the necessary quantities (i.e., λL_{5100}, M_{BH}, σ) for that study were only accessible for these 79 objects.

2.2. SDSS Observations and Data Reduction

SDSS spectra are obtained from a 2.5 m ground-based telescope with a $3''$ diameter circular optical fiber and an exposure time of 54 s. SDSS spectra cover a wavelength range of 3800–9200 Å with an instrumental resolution of 170 km s^{-1}. SDSS data are already fully reduced and flux calibrated when retrieved from the SDSS archive.

2.3. Keck Observations and Data Reduction

The 102 objects selected from SDSS were observed again between 2009 January and 2010 March with the Low Resolution Imaging Spectrometer (LRIS) at the Keck 10 m telescope using a $1'' \times 2''$ wide rectangular longslit aligned with the major axis of the host galaxy (given by SDSS). While all objects were observed at as low an airmass as possible, given observation constraints the airmass for individual objects can be as high as 1.4. Objects observed in 2009 used a D560 dichroic and objects observed in 2010 used a D680 dichroic. The blue Keck spectra were taken with the 600/400 grism giving a wavelength range of ~3200–5350 Å and an instrumental resolution of ~90 km s^{-1}; the red spectra were taken with the 831/8200 grating centered on 8950 Å with a resolution of ~45 km s^{-1}. (Note that the red Keck spectra are not used in this paper since they only cover the Ca triplet absorption lines for an accurate measurement of σ). The exposure times generally range from 600 to 1200 s. Keck

spectra were taken on average 6.4 ± 1.8 years after the SDSS spectra, ranging from 2.6 to 9.1 years (see Table 2 for details on SDSS and Keck observations).

The Keck data are reduced following standard reduction steps such as bias subtraction, flat field correcting, cosmic ray rejection, and wavelength calibration. AOV *Hipparcos* stars were used to correct for telluric absorption and relative flux calibration. Note that unlike SDSS spectra, Keck spectra are not absolute flux calibrated because observing conditions were typically not photometric. 1D spectra were extracted from the 2D spectra with a width of $1''08$ (8 pixels) to encompass the BLR, given the slit width of $1''$ and a typical seeing of $1''$.

2.4. Lick Observations and Data Reduction

For eight objects with significantly weaker or apparently absent broad Hβ emission in the Keck spectra, follow-up observations were conducted in 2013 January and March with the 3 m Shane telescope of Lick observatory using the Kast spectrograph and 60 minutes total exposure time per object. (Table 2; Scott 2013). The slit was aligned either along the major axis or perpendicular to it. 1D spectra were extracted using a 4 pixel ($\approx 3''$) width centered on the peak flux to mimic the $3''$ diameter circular fiber of SDSS. The data were reduced following standard procedures. The Lick spectra are presented by Scott (2013). These spectra are used to determine their Seyfert type, since they also cover the Hα region. The Seyfert types based on the Lick spectra are listed in Table 2.

3. ANALYSIS

In this paper we focus on four different sets of spectra, for short called "Keck subtracted," "Keck unsubtracted," "SDSS subtracted," and "SDSS unsubtracted," as explained in the next two sections.

3.1. Unsubtracted Spectra

To classify Seyfert type and perform a qualitative comparison of the Hβ region, the reduced spectra are used. Throughout the paper these spectra are referred to as the unsubtracted data set.

For a visual comparison of both data sets (Figures 3–6), the Keck spectra were re-binned to match the lower spectral resolution of the SDSS spectra. Moreover, the spectra were normalized to constant 5007 Å [O III] emission, assuming that the 5007 Å [O III] emission line flux is identical in both data sets, given that emission from the extended NLR does not vary over the observed timescales. This scaling also assumes that both spectra integrate the same [O III] emission over the same area, which might not necessarily be the case given the different apertures used. Aligning the long Keck slit along the major axis of the host galaxy may reduce any difference in [O III] flux covered. However, we discuss aperture effects in more detail below.

3.2. Hβ Fitting and Subtracted Spectra

A multi-component spectral decomposition is used to fit the region around Hβ. The procedure is summarized here briefly (see Park et al. 2015 for details).

First, the observed continuum is modeled and subtracted by fitting a pseudo-continuum consisting of the featureless AGN power-law continuum, host galaxy starlight templates from the
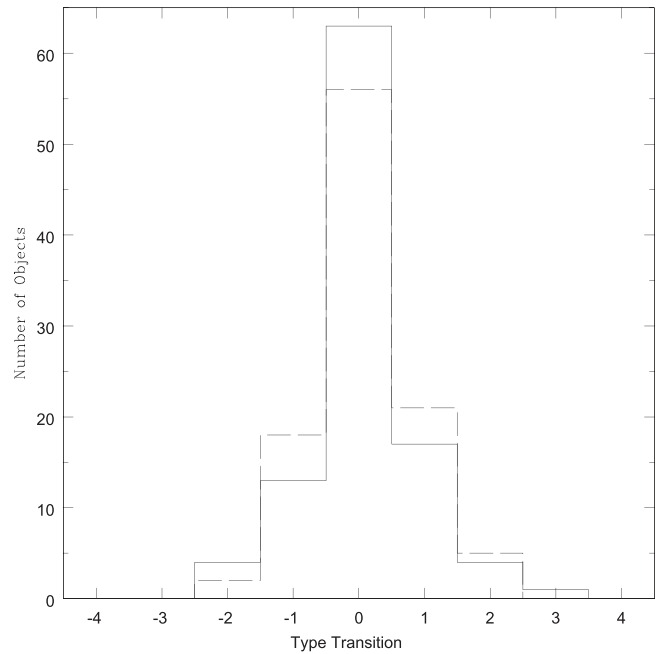

Figure 1. Magnitude of Seyfert-type transitions from visual classification (solid line) and peak flux ratio (dashed line; see the text for details).

Indo-US spectral library (Valdez et al. 2004), and the AGN Fe II emission template from Boroson & Green (1992) for the Keck spectra and from Kovacevic et al. (2010) for the SDSS spectra.[7] Then the continuum-subtracted Hβ line region is modeled by fitting Gauss–Hermite series (van der Marel & Franx 1993; Woo et al. 2006; McGill et al. 2008) simultaneously to the [O III] narrow emission lines $\lambda\lambda4959$, 5007 Å and the broad and narrow Hβ lines, to allow for the fitting of asymmetries. Gauss–Hermite polynomials of order 3–6 are used to fit the broad Hβ line and 7–12 for each [O III] line. In cases where the He II $\lambda4686$ Å emission line is blended with the broad Hβ, the broad and narrow He II were fitted by simple Gaussian functions.

Depending on the degree of overlap of the broad Hβ component with the [O III] lines, we model the Hβ line region in two slightly different ways. If there is no blending between the broad Hβ component and the [O III]$\lambda5007$ Å line, we create a template for the narrow-line components by fitting the [O III] $\lambda5007$ Å line with a Gauss–Hermite series function. The [O III] $\lambda4959$ Å line is then subtracted by blueshifting the template with a flux scale ratio fixed to 1:3 (see, e.g., Dimitrijević et al. 2007, and references therein). Then, the broad and narrow Hβ components are fitted simultaneously through χ^2-minimization, using the blueshifted template from the [O III] $\lambda5007$ Å line as a template for the narrow Hβ, with the flux ratio as a free parameter, and a Gauss–Hermite series for the broad Hβ component.

If the broad Hβ component is heavily blended with the [O III] doublet lines, we model the Hβ broad and narrow lines and the [O III]$\lambda\lambda4959$, 5007 Å lines all together by simultaneously fitting a Gauss–Hermite series function to the broad Hβ

---

[7] The two different Fe II templates are being used due to the different wavelength ranges covered by the Keck and SDSS spectra. The Keck spectra do not extend far enough into the red to fit the Fe II features around 5200 Å with the Kovacevic et al. (2010) multi-component template and instead must be fitted with the monolithic template from Boroson & Green (1992).

component and another Gauss–Hermite series function to the [O III]λ5007 Å line, where the model for the [O III]λ5007 Å line is blueshifted and also used for both the [O III]λ4959 Å line with a 1:3 flux scale ratio and the narrow Hβ component with a free flux scale ratio. This approach is based on the known fixed flux ratio of [O III] $\lambda\lambda$4959, 5007 of 1:3 and the fact that the [O III] lines and the narrow Hβ lines originate in the NLR and should have comparable widths. It is an approach typically used to fit AGN spectra in, e.g., reverberation mapping studies (Barth et al. 2015; Park et al. 2015).

The results of the spectral fitting are given in Table 3 and the fits are shown in Figures 7–10. The pure emission line spectra —with host galaxy, power-law continuum and Fe II emission subtracted—are referred to in the following as the subtracted data.

Note that for one object in the sample (1655+2014), the signal-to-noise ratio (S/N) is too low in both the SDSS and the Keck spectra for an accurate measurement of the broad Hβ line. For three other objects (0932+0405, 0847+1824, and 0831 +0521), the broad Hβ component could not be accurately identified in the Keck spectra. These four objects are excluded from any discussion involving the Hβ line fitting.

3.3. Seyfert-type Classification

The Seyfert type for all objects was classified independently by eye by two members of the team (J.N.R. and M.C.) following Table 1, and has been verified independently by the broad Hβ emission line fitting results. Table 2 lists the Seyfert-type classifications for both SDSS and Keck spectra as well as the eight objects observed at Lick. Typically the Hα and Hβ lines are used for Seyfert-type classification and we followed that procedure for the SDSS and Lick spectra. However, the Keck spectra do not extend to the Hα line. Instead, higher-order Balmer lines (Hγ and Hδ) were used as a proxy (see Table 1) (Osterbrock 1977). However, these lines are intrinsically much fainter than Hα and Hβ; for example, assuming case B recombination, Hδ (Hγ) is ~26% (47%) the strength of Hβ which itself is approximately 35% of Hα (Osterbrock 1989). Moreover, the Hγ line is often blended with the 4383 Å Fe I and the 4363 Å [O III] lines, cautioning the use of this line for classification. Thus, we rely on the Hβ line for classification. This implies that we cannot differentiate between types-1.9 and 2 for Keck spectra. We conservatively classify an object without a broad Hβ line in the Keck spectra as a type-1.9. Note that given the lower S/N of the SDSS spectra, caution should be exercised when classifying the Seyfert sub-types (1.5, 1.8, and 1.9) since broad lines can be easily lost in the noise. However, given that these are all local Seyfert galaxies, generally, S/N are good even for the SDSS spectra. The observed variability of the broad Hβ line is substantial and the overall trend is for a weaker broad Hβ line in Keck, partially due to selection effects (see discussion below).

For a more quantitative determination of Seyfert type, we used the Hβ broad/narrow peak flux ratios and compared them to the visual classification. The reason for choosing peak flux ratios are threefold: (i) using flux ratios eliminates uncertainties on absolute flux calibration; (ii) moreover, compared with integrated flux ratios, peak flux ratios are essentially driving the visual classification scheme; and (iii) the width of the broad Hβ line can have large uncertainties and depends strongly on the placement of the continuum. Depending on the S/N of the data, it can easily be either lost in the noise or noise can be fitted as a
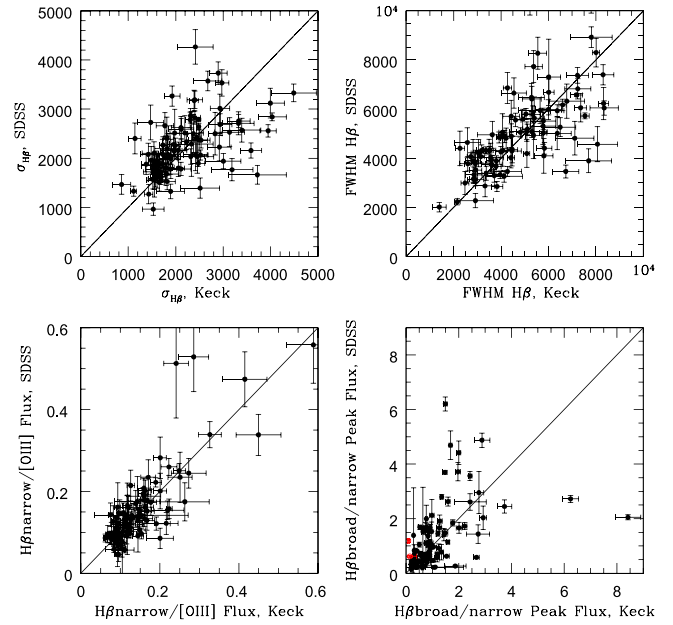

Figure 2. Derived quantities from Hβ line fitting of SDSS spectra (y-axis) vs. Keck spectra (x-axis; including a unity line). Top left: $\sigma_{H\beta}$. Top right: FWHM$_{H\beta}$. Bottom left: Hβ_{narrow}/[O III] flux ratio. Bottom right: Hβ_{broad}/Hβ_{narrow} peak flux ratio. The two objects shown in red in this panel were classified as 1.9 in the Keck spectrum, thus they do not have a broad component in Hβ and this comparison uses an upper limit on the flux if a broad component were included.

broad Hβ line. Thus, integrated flux ratios are more uncertain than peak flux ratios.

While there is scatter between these two different classification approaches, we determined cutoffs in the Hβ broad/narrow peak flux ratios by minimizing the number of outliers. For a peak flux ratio $\geqslant$ 1.25, there is an 83% chance that the object is a type-1; for a 1.25 $\geqslant$ peak flux ratio $\geqslant$ 0.6, there is a 67% chance that the object is a type-1.5; and for a peak flux ratio $\leqslant$ 0.6, there is a 72% change that the object is a type-1.8. All type-1.9 objects have a peak flux ratio of 0, since there is no broad Hβ component. In Section 4.1 we discuss the results based on both visual classification as well as peak flux ratios. The peak flux ratios are given in Table 2.

4. RESULTS AND DISCUSSION

4.1. Seyfert-type Transitions

Based on our visual classifications, at least some degree of type transition is exhibited by 39/102 objects (39 ± 10%). To quantify the "magnitude" of the transition, we assign a value between +4 and −4 in increments of 1, with a positive value if the broad Hβ line weakened between SDSS and Keck. Type changes of +4 indicate a full type transition from type-1 to 2; +3 indicates the object transitioned three types (e.g., 1–1.9); +2 indicates a transition of two types (e.g., 1–1.8); and +1 indicates a transition of one type (e.g., 1–1.5); 0 indicates that the object did not experience a Seyfert-type change. A negative value implies that the Hβ line increased between SDSS and Keck. Figure 1 shows the distribution of the type transitions quantified in this way.

While there are type transitions in either direction, there are more objects that transition toward a narrower/weaker broad Hβ line in Keck (transition toward type-2) which is likely a reflection of our sample selection, since only Seyfert galaxies

Table 2
Observations and Seyfert-type Classification

Object	R.A. (J2000)	decl. (J2000)	z	Date SDSS	Class. SDSS	Date Keck	Class. Keck	Exp. Time Keck (s)	Diff. years	Date Lick	Class. Lick
(1)	(2)	(3)	(4)	(5)	(6)	(7)	(8)	(9)	(10)	(11)	(12)
0013−0951	00 13 35.38	−09 51 20.9	0.062	2001 Aug 17 (52138)	1	2009 Sep 20 (55094)	1.5	600	8.09	⋯	⋯
0026+0009	00 26 21.29	+00 09 14.9	0.060	2000 Aug 26 (51782)	1	2009 Sep 20 (55094)	1	1600	9.07	⋯	⋯
0038+0034	00 38 47.96	+00 34 57.5	0.081	2000 Sep 06 (51793)	1	2009 Sep 20 (55094)	1.5	600	9.04	⋯	⋯
0109+0059	01 09 39.01	+00 59 50.4	0.093	2000 Sep 07 (51794)	1.5	2009 Sep 20 (55094)	1.5	600	9.04	⋯	⋯
0121−0102	01 21 59.81	−01 02 24.4	0.054	2000 Sep 02 (51789)	1.5	2009 Jan 21 (54852)	1	1200	8.39	⋯	⋯
0150+0057	01 50 16.43	+00 57 01.9	0.085	2000 Sep 06 (51793)	1	2009 Sep 20 (55094)	1	600	9.04	⋯	⋯
0206−0017	02 06 15.98	−00 17 29.1	0.043	2000 Sep 25 (51812)	1	2009 Jan 22 (54853)	1	1200	8.33	⋯	⋯
0212+1406	02 12 57.59	+14 06 10.0	0.062	2000 Dec 05 (51883)	1	2009 Sep 20 (55094)	1	600	8.79	⋯	⋯
0301+0110	03 01 24.26	+01 10 22.5	0.072	2000 Sep 30 (51817)	1.5	2009 Sep 20 (55094)	1.5	600	8.97	⋯	⋯
0301+0115	03 01 44.19	+01 15 30.8	0.075	2000 Sep 30 (51817)	1	2009 Sep 20 (55094)	1	600	8.97	⋯	⋯
0310−0049	03 10 27.82	−00 49 50.7	0.080	2001 Dec 15 (52258)	1	2009 Sep 20 (55094)	1	600	7.76	⋯	⋯
0336−0706	03 36 02.09	−07 06 17.1	0.097	2000 Dec 31 (51909)	1.8	2009 Sep 20 (55094)	1.8	2400	8.72	⋯	⋯
0353−0623	03 53 01.02	−06 23 26.3	0.076	2000 Dec 30 (51908)	1.8	2009 Jan 22 (54853)	1	1200	8.06	⋯	⋯
0731+4522	07 31 26.68	+45 22 17.4	0.092	2004 Nov 05 (53314)	1.5	2009 Sep 20 (55094)	1.5	600	4.87	⋯	⋯
0735+3752	07 35 21.19	+37 52 01.9	0.096	2000 Nov 29 (51877)	1.5	2009 Sep 20 (55094)	1.8	600	8.81	⋯	⋯
0737+4244	07 37 03.28	+42 44 14.6	0.088	2004 Jan 31 (53035)	1.5	2009 Sep 20 (55094)	1.5	600	5.64	⋯	⋯
0802+3104	08 02 43.40	+31 04 03.3	0.041	2003 Jan 02 (52641)	1	2009 Jan 21 (54852)	1	1200	5.97	⋯	⋯
0811+1739	08 11 10.28	+17 39 43.9	0.065	2004 Dec 18 (53357)	1.5	2010 Mar 15 (55270)	1	2700	5.24	⋯	⋯
0813+4608	08 13 19.34	+46 08 49.5	0.054	2000 Nov 29 (51877)	1.8	2010 Jan 14 (55210)	1	1200	9.13	⋯	⋯
0831+0521	08 31 07.62	+05 21 05.9	0.035	2003 Jan 07 (52646)	1.8	2010 Mar 15 (55270)	1.9	600	7.18	⋯	⋯
0845+3409	08 45 56.67	+34 09 36.3	0.066	2003 Feb 02 (52672)	1.5	2010 Mar 14 (55269)	1.5	3600	7.11	⋯	⋯
0846+2522	08 46 54.09	+25 22 12.3	0.051	2004 Dec 19 (53358)	1.5	2009 Jan 22 (54853)	1.5	1200	4.09	⋯	⋯
0847+1824	08 47 48.28	+18 24 39.9	0.085	2005 Dec 07 (53711)	1	2009 Jan 21 (54852)	1.9	1200	3.10	2013 Jan 15 (56307)	2
0854+1741	08 54 39.25	+17 41 22.5	0.065	2005 Dec 25 (53729)	1.5	2010 Mar 15 (55270)	1	600	4.22	⋯	⋯
0857+0528	08 57 37.77	+05 28 21.3	0.059	2003 Jan 31 (52670)	1	2010 Jan 15 (55211)	1	600	6.96	⋯	⋯
0904+5536	09 04 36.95	+55 36 02.5	0.037	2000 Dec 30 (51908)	1.5	2010 Mar 14 (55269)	1.5	600	9.20	⋯	⋯
0909+1330	09 09 02.35	+13 30 19.4	0.051	2006 Apr 01 (53826)	1.8	2010 Jan 14 (55210)	1	600	3.79	⋯	⋯
0921+1017	09 21 15.55	+10 17 40.9	0.039	2004 Feb 15 (53050)	1.8	2010 Jan 14 (55210)	1.8	700	5.91	⋯	⋯
0923+2254	09 23 43.00	+22 54 32.7	0.033	2005 Dec 23 (53727)	1	2010 Jan 15 (55211)	1	600	4.06	⋯	⋯
0923+2946	09 23 19.73	+29 46 09.1	0.063	2005 Jan 19 (53389)	1.8	2010 Jan 15 (55211)	1.8	600	4.99	⋯	⋯
0927+2301	09 27 18.51	+23 01 12.3	0.026	2005 Dec 26 (53730)	1.5	2010 Jan 15 (55211)	1.5	600	4.05	⋯	⋯

Table 2
(Continued)

Object	R.A. (J2000)	decl. (J2000)	z	Date SDSS	Class. SDSS	Date Keck	Class. Keck	Exp. Time Keck (s)	Diff. years	Date Lick	Class. Lick
(1)	(2)	(3)	(4)	(5)	(6)	(7)	(8)	(9)	(10)	(11)	(12)
0932+0233	09 32 40.55	+02 33 32.6	0.057	2001 Feb 25 (51965)	1.8	2010 Jan 14 (55210)	1.5	600	8.88	⋯	⋯
0932+0405	09 32 59.60	+04 05 06.0	0.059	2001 Dec 21 (52264)	1.8	2010 Jan 14 (55210)	1.9	600	8.07	2013 Mar 11 (56362)	1.9
0936+1014	09 36 41.08	+10 14 15.7	0.060	2003 Dec 20 (52993)	1.5	2010 Mar 15 (55270)	1	3600	6.23	⋯	⋯
0938+0743	09 38 12.27	+07 43 40.0	0.022	2003 Apr 04 (52733)	1	2010 Jan 14 (55210)	1.8	600	6.78	2013 Jan 15 (56307)	1.8
0948+4030	09 48 38.43	+40 30 43.5	0.047	2003 Mar 11 (52709)	1	2010 Jan 15 (55211)	1.8	900	6.85	⋯	⋯
1002+2648	10 02 18.79	+26 48 05.7	0.052	2006 Jan 22 (53757)	1.8	2010 Jan 15 (55211)	1.9	600	3.98	⋯	⋯
1029+1408	10 29 25.73	+14 08 23.2	0.061	2004 Mar 11 (53075)	1.5	2010 Jan 15 (55211)	1.5	600	5.85	⋯	⋯
1029+2728	10 29 01.63	+27 28 51.2	0.038	2006 Feb 28 (53794)	1.8	2010 Jan 15 (55211)	1.8	600	3.88	⋯	⋯
1029+4019	10 29 46.80	+40 19 13.8	0.067	2004 Jan 29 (53033)	1.5	2010 Jan 14 (55210)	1.5	600	5.96	⋯	⋯
1038+4658	10 38 33.42	+46 58 06.6	0.063	2002 Dec 12 (52620)	1.5	2010 Jan 14 (55210)	1.9	600	7.09	2013 Jan 17 (56309)	1.9
1042+0414	10 42 52.94	+04 14 41.1	0.052	2002 Mar 06 (52339)	1.5	2009 Apr 16 (54937)	1.5	1200	7.11	⋯	⋯
1043+1105	10 43 26.47	+11 05 24.3	0.048	2004 Apr 20 (53115)	1.8	2009 Apr 16 (54937)	1.8	600	4.99	⋯	⋯
1049+2451	10 49 25.39	+24 51 23.7	0.055	2006 Feb 26 (53792)	1	2009 Apr 16 (54937)	1	600	3.13	⋯	⋯
1058+5259	10 58 28.76	+52 59 29.0	0.068	2003 Jan 13 (52652)	1.5	2010 Jan 14 (55210)	1.5	600	7.00	⋯	⋯
1101+1102	11 01 01.78	+11 02 48.8	0.036	2004 Apr 24 (53119)	1.5	2009 Apr 16 (54937)	1.8	600	4.98	⋯	⋯
1104+4334	11 04 56.03	+43 34 09.1	0.049	2004 Feb 18 (53053)	1.8	2010 Jan 14 (55210)	1.5	600	5.91	⋯	⋯
1110+1136	11 10 45.97	+11 36 41.7	0.042	2004 Mar 14 (53078)	1.5	2010 Mar 15 (55270)	1	3600	6.00	⋯	⋯
1116+4123	11 16 07.65	+41 23 53.2	0.021	2003 Dec 30 (53003)	1.8	2009 Apr 15 (54936)	1.8	850	5.29	⋯	⋯
1118+2827	11 18 53.02	+28 27 57.6	0.060	2006 Feb 27 (53793)	1.8	2010 Jan 15 (55211)	1.9	900	3.88	2013 Mar 11 (56362)	1.8
1132+1017	11 32 49.28	+10 17 47.4	0.044	2003 May 22 (52781)	1.5	2010 Jan 15 (55211)	1	600	6.65	⋯	⋯
1137+4826	11 37 04.17	+48 26 59.2	0.054	2003 Jan 03 (52642)	1.5	2010 Jan 14 (55210)	1.5	600	7.03	⋯	⋯
1139+5911	11 39 08.95	+59 11 54.6	0.061	2002 May 15 (52409)	1	2010 Jan 14 (55210)	1	600	7.67	⋯	⋯
1140+2307	11 40 54.09	+23 07 44.4	0.035	2006 May 21 (53876)	1.8	2010 Jan 15 (55211)	1.8	1200	3.66	2013 Jan 13 (56305)	2
1143+5941	11 43 44.30	+59 41 12.4	0.063	2002 May 17 (52411)	1.5	2010 Mar 14 (55269)	1	3000	7.82	⋯	⋯
1144+3653	11 44 29.88	+36 53 08.5	0.038	2005 Mar 13 (53442)	1	2009 Apr 16 (54937)	1	600	4.09	⋯	⋯
1145+5547	11 45 45.18	+55 47 59.6	0.053	2003 Apr 30 (52759)	1	2010 Mar 14 (55269)	1	3600	6.87	⋯	⋯
1147+0902	11 47 55.08	+09 02 28.8	0.069	2003 May 01 (52760)	1.5	2010 Jan 15 (55211)	1.5	600	6.71	⋯	⋯
1205+4959	12 05 56.01	+49 59 56.4	0.063	2002 Jun 17 (52442)	1.8	2010 Jan 14 (55210)	1.8	600	7.58	⋯	⋯
1206+4244	12 06 26.29	+42 44 26.1	0.052	2004 Apr 25 (53120)	1	2010 Mar 14 (55269)	1	1100	5.88	⋯	⋯
1210+3820	12 10 44.27	+38 20 10.3	0.023	2005 Apr 13 (53473)	1.5	2009 Apr 16 (54937)	1.5	600	4.01	⋯	⋯
1216+5049	12 16 07.09	+50 49 30.0	0.031	2002 May 19 (52413)	1.8	2010 Mar 14 (55269)	1.8	900	6.82	⋯	⋯

Table 2
(Continued)

Object (1)	R.A. (J2000) (2)	decl. (J2000) (3)	z (4)	Date SDSS (5)	Class. SDSS (6)	Date Keck (7)	Class. Keck (8)	Exp. Time Keck (s) (9)	Diff. years (10)	Date Lick (11)	Class. Lick (12)
1223+0240	12 23 24.14	+02 40 44.4	0.024	2002 Jan 09 (52283)	1	2010 Mar 15 (55270)	1	600	8.18	⋯	⋯
1228+0951	12 28 11.41	+09 51 26.7	0.064	2003 Apr 02 (52731)	1.8	2010 Mar 15 (55270)	1.8	600	6.95	⋯	⋯
1231+4504	12 31 52.04	+45 04 42.9	0.062	2004 Feb 27 (53062)	1.5	2010 Jan 15 (55211)	1.5	1200	5.88	⋯	⋯
1241+3722	12 41 29.42	+37 22 01.9	0.063	2006 Apr 02 (53827)	1.5	2010 Jan 15 (55211)	1.5	800	3.79	⋯	⋯
1246+5134	12 46 38.74	+51 34 55.9	0.067	2002 Apr 15 (52379)	1.8	2010 Jan 15 (55211)	1.5	600	7.75	⋯	⋯
1250−0249	12 50 42.44	−02 49 31.5	0.047	2001 Mar 29 (51997)	1.5	2009 Apr 16 (54937)	1.8	1200	8.05	⋯	⋯
1306+4552	13 06 19.83	+45 52 24.2	0.051	2004 Apr 22 (53117)	1	2010 Mar 14 (55269)	1.5	3600	5.89	⋯	⋯
1307+0952	13 07 21.93	+09 52 09.3	0.049	2006 May 29 (53884)	1.8	2010 Mar 15 (55270)	1.5	2400	3.79	⋯	⋯
1312+2628	13 12 59.59	+26 28 24.0	0.060	2006 Feb 28 (53794)	1	2010 Mar 14 (55269)	1	2700	4.04	⋯	⋯
1313+3653	13 13 48.96	+36 53 57.9	0.067	2006 Mar 21 (53815)	1.8	2010 Mar 14 (55269)	1.8	600	3.98	⋯	⋯
1323+2701	13 23 10.39	+27 01 40.4	0.056	2006 Mar 01 (53795)	1.8	2009 Apr 16 (54937)	1.8	700	3.13	⋯	⋯
1353+3951	13 53 45.93	+39 51 01.6	0.063	2004 Feb 26 (53061)	1.8	2010 Mar 14 (55269)	1.9	600	6.05	2013 Mar 12 (56363)	1.8
1355+3834	13 55 53.52	+38 34 28.5	0.050	2005 Mar 31 (53460)	1.8	2009 Apr 16 (54937)	1.8	300	4.04	⋯	⋯
1405−0259	14 05 14.86	−02 59 01.2	0.054	2002 Jun 18 (52443)	1	2009 Apr 16 (54937)	1	1600	6.83	⋯	⋯
1416+0317	14 16 30.82	+01 37 07.9	0.054	2001 Mar 26 (51994)	1.5	2010 Mar 15 (55270)	1.8	2700	8.97	⋯	⋯
1419+0754	14 19 08.30	+07 54 49.6	0.056	2005 Jun 12 (53533)	1.8	2009 Apr 16 (54937)	1.8	900	3.84	⋯	⋯
1423+2720	14 23 38.43	+27 20 09.7	0.064	2006 May 26 (53881)	1.5	2010 Mar 14 (55269)	1.9	1200	3.80	2013 Mar 12 (56363)	1.8
1434+4839	14 34 52.45	+48 39 42.8	0.037	2003 Apr 04 (52733)	1	2009 Apr 16 (54937)	1.5	600	6.03	⋯	⋯
1505+0342	15 05 56.55	+03 42 26.3	0.036	2001 May 26 (52055)	1.5	2010 Mar 15 (55270)	1.5	1200	8.80	⋯	⋯
1535+5754	15 35 52.40	+57 54 09.3	0.030	2002 Mar 14 (52347)	1	2009 Apr 15 (54936)	1	1200	7.09	⋯	⋯
1543+3631	15 43 51.49	+36 31 36.7	0.067	2003 Aug 24 (52875)	1	2010 Mar 15 (55270)	1.5	1200	6.56	⋯	⋯
1545+1709	15 45 07.53	+17 09 51.1	0.048	2006 Jun 03 (53889)	1.8	2009 Apr 15 (54936)	1	1200	2.57	⋯	⋯
1554+3238	15 54 17.42	+32 38 37.6	0.048	2003 Jul 05 (52825)	1.5	2009 Apr 15 (54936)	1.5	1200	5.78	⋯	⋯
1557+0830	15 57 33.13	+08 30 42.9	0.047	2004 Aug 11 (53228)	1.5	2009 Apr 15 (54936)	1.5	1200	4.68	⋯	⋯
1605+3305	16 05 02.46	+33 05 44.8	0.053	2004 May 17 (53142)	1	2009 Apr 15 (54936)	1	1200	4.91	⋯	⋯
1606+3324	16 06 55.94	+33 24 00.3	0.059	2004 May 19 (53144)	1.5	2009 Apr 15 (54936)	1.5	1200	4.91	⋯	⋯
1611+5211	16 11 56.30	+52 11 16.8	0.041	2001 May 22 (52051)	1.5	2009 Apr 15 (54936)	1.8	1200	7.95	⋯	⋯
1636+4202	16 36 31.28	+42 02 42.5	0.061	2001 Jun 23 (52083)	1	2010 Mar 14 (55269)	1	1200	8.72	⋯	⋯
1647+4442	16 47 21.47	+44 42 09.7	0.025	2001 May 22 (52051)	1.8	2010 Mar 14 (55269)	1.5	4200	8.81	⋯	⋯
1655+2014	16 55 14.21	+20 14 42.0	0.084	2004 Jun 13 (53169)	1.8	2009 Sep 20 (55094)	1.8	600	5.27	⋯	⋯
1708+2153	17 08 59.15	+21 53 08.1	0.072	2004 Jun 21 (53177)	1.5	2009 Sep 20 (55094)	1	600	5.25	⋯	⋯

Table 2
(Continued)

Object (1)	R.A. (J2000) (2)	decl. (J2000) (3)	z (4)	Date SDSS (5)	Class. SDSS (6)	Date Keck (7)	Class. Keck (8)	Exp. Time Keck (s) (9)	Diff. years (10)	Date Lick (11)	Class. Lick (12)
2116+1102	21 16 46.33	+11 02 37.3	0.081	2002 Jul 13 (52468)	1.8	2009 Sep 20 (55094)	1.8	700	7.19	⋯	⋯
2140+0025	21 40 54.55	+00 25 38.2	0.084	2002 Jul 10 (52465)	1	2009 Sep 20 (55094)	1	600	7.20	⋯	⋯
2215−0036	22 15 42.29	−00 36 09.6	0.099	2000 Sep 04 (51791)	1	2009 Sep 20 (55094)	1	600	9.04	⋯	⋯
2221−0906	22 21 10.83	−09 06 22.0	0.091	2001 Oct 21 (52203)	1	2009 Sep 20 (55094)	1	600	7.92	⋯	⋯
2222−0819	22 22 46.61	−08 19 43.9	0.082	2001 Oct 24 (52206)	1.5	2009 Sep 20 (55094)	1.5	700	7.91	⋯	⋯
2233+1312	22 33 38.42	+13 12 43.5	0.093	2002 Sep 04 (52521)	1	2009 Sep 20 (55094)	1.5	800	7.04	⋯	⋯
2254+0046	22 54 52.24	+00 46 31.4	0.091	2000 Sep 02 (51789)	1	2009 Sep 20 (55094)	1	600	9.05	⋯	⋯
2327+1524	23 27 21.97	+15 24 37.4	0.046	2001 Nov 25 (52238)	1.5	2009 Sep 20 (55094)	1.8	600	7.82	⋯	⋯
2351+1552	23 51 28.75	+15 52 59.1	0.096	2001 Nov 13 (52226)	1.8	2009 Sep 20 (55094)	1.8	600	7.85	⋯	⋯

Note. Column (1): target ID based on R.A. and decl. used throughout the text. Column (2): R.A. Column (3): decl. Column (4): redshift from SDSS-DR7. Column (5): date on which SDSS spectrum was taken (with Modified Julian Date (MJD) in brackets). Column (6): Seyfert-type classification based on SDSS spectrum. Column (7): date on which Keck spectrum was taken (with MJD in brackets). Column (8): Seyfert-type classification based on Keck spectrum. Note that because Keck spectra do not extend to Hα, we cannot differentiate between type-1.9 and type-2, and conservatively classify these objects in question as type-1.9. Column (9): exposure time of Keck observations in seconds. Note that the exposure time for all SDSS spectra is 54 s. Column (10): time between SDSS and Keck observations in years. Column (11): date on which Lick spectrum was taken (with MJD in brackets). Column (12): Seyfert-type classification based on Lick spectrum.

with a broad Hβ component were selected from SDSS (Bennert et al. 2011; Harris et al. 2012). Of the 39 objects with a type transition, the majority (31) experiences only a minor type change (± 1 mag transition), while eight underwent greater type changes of 2. One object (0847+1824) demonstrated a type transition of magnitude 3. We consider three objects (3% of the sample) extreme objects since they all show cases of a disappearing broad Hβ line between SDSS and Keck. We discuss them in detail in Section 4.3. There is no correlation between the magnitude of the type transition and the time between observations, indicating that a Seyfert-type change happens on shorter timescales than those covered by our observations (6.4 $\pm$ 1.8 years).

If we instead use our peak flux ratio cutoffs as discussed in Section 4.1 to classify the Seyfert type, the results change only slightly: 46/102 objects undergo a type transition, with the majority (39) experiencing only a minor type change (± 1 magnitude transition), while seven underwent greater type changes of 2. However, we consider the visual classification more reliable and it is also commonly used in the literature. Thus, in the following we refer to the visual classification.

As outlined in the introduction, AGN type changes have previously been observed in the literature and are often referred to as "changing look" AGNs (see, e.g., Denney et al. 2014; LaMassa et al. 2015; Runnoe et al. 2016, and references therein); indeed, the frequency and strength of our observed Hβ emission line variability is in line with one of the first studies on this topic (Rosenblatt et al. 1994).

Two common explanations of type transitions are variable accretion and variable obscuration. Variable accretion, caused by fluctuating amounts of gas available to feed the BH

(Bochkarev 2006), results in a change of the continuum flux and subsequently in a change of the broad Hβ emission line flux since the BLR clouds are photoionized by the UV continuum. There are many papers citing variable accretion as the driving force behind Seyfert-type transitions (Eracleous & Halpern 2001; Trippe et al. 2008; Denney et al. 2014; Shappee et al. 2014). Denney et al. (2014) is the most notable example reporting Mrk 590 transitioning from type-1.5 to type-1, then transitioning again to type $\sim$1.9–2. Shappee et al. (2014) (for NGC 2617), Trippe et al. (2008) (for NGC 2992), and Antonucci & Cohen (1983) (for NGC 4151) report an observed change in X-ray flux that is followed by a similar change in UV/optical flux. Variable extinction can occur when dusty clouds pass our line of sight. For Seyfert galaxies, the source of this obscuration is likely the dusty torus, thought to surround the BLR in the framework of the standard unified model. The individual cold gas clouds of the dusty torus are not all identical and uniform, so different gas clouds could shield different amounts of continuum and Hβ flux.

The disappearance of broad lines as seen in 3% of our sample (discussed in detail in Section 4.3) has also been documented before. In particular, Ho & Kim (2009) report that ten of the 94 objects in their local sample ($\sim$11%), selected to investigate relationships between M_{BH} and host galaxy properties using *Magellan* spectra (3600–6000 Å wavelength range), had only narrow lines when the same objects were previously classified as type-1 Seyferts. (Note that Ho & Kim 2009 do not discuss this matter further since it was not the main purpose of their paper.)

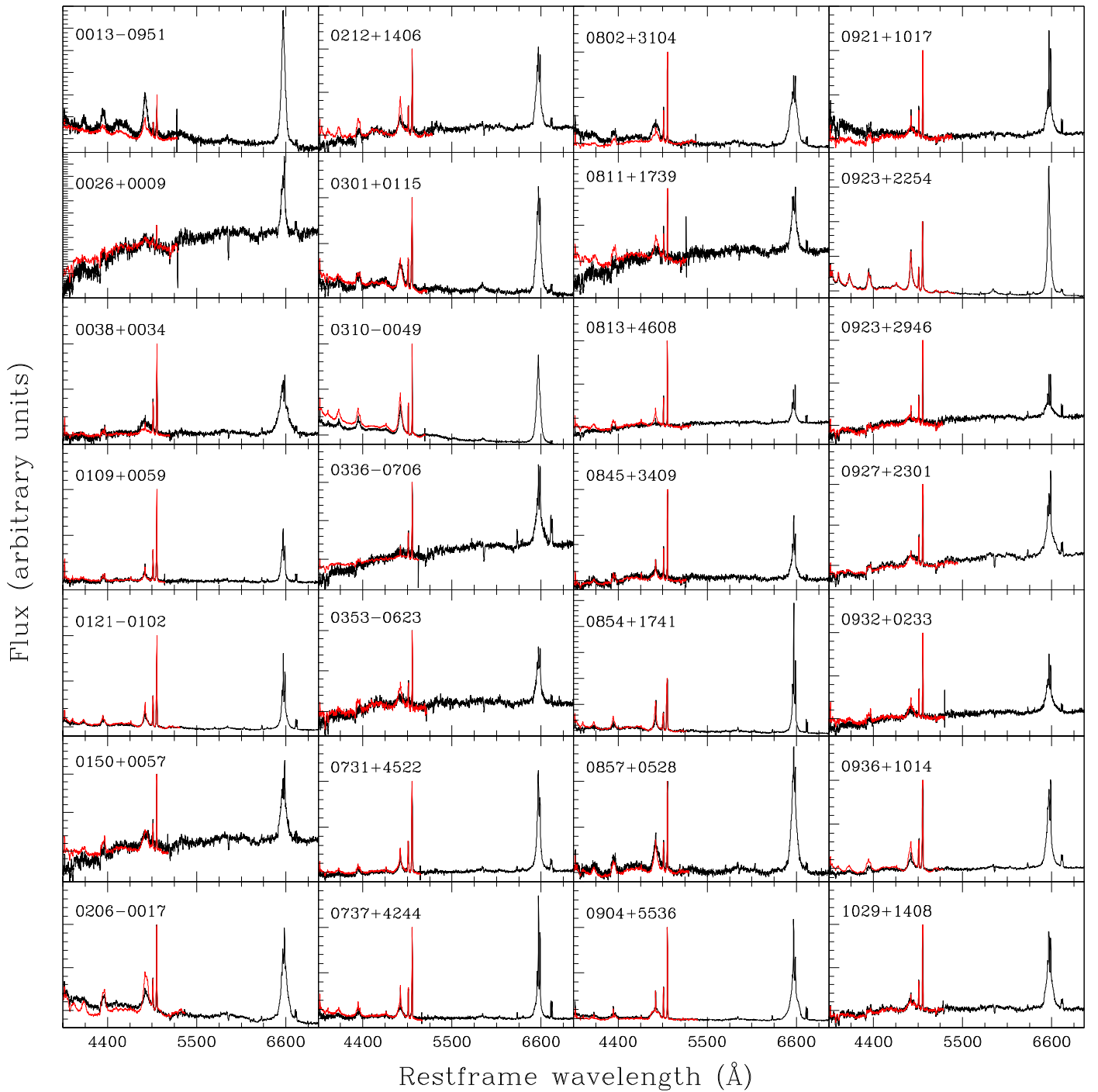In a sample of 117 changing look quasar candidates selected from SDSS DR12, Ruan et al. (2015) discover two new low-

Figure 3. Unsubtracted spectra comparing SDSS (black) and Keck (red) (3850–7000 Å). Note that the Keck spectra only cover the blue part. For comparison, the Keck spectra were re-binned to match the lower spectral resolution of the SDSS spectra. Moreover, for both spectra, the base of the 5007 Å [O III] line was set to 0 and the peak to 1 (see text for discussion). Objects shown in this figure are included in Bennert et al. (2015).

redshift quasars (in addition to the one previously found by LaMassa et al. 2015) where both the broad Hβ and continuum luminosity dim over the five to seven years in rest-frame time, changing the objects from quasar-like to galaxy-like states. Ruan et al. (2015) argue that the observed change is driven by rapidly decreasing accretion rates.

From a sample of 1011 low-redshift quasars ($z < 0.63$) selected based on repeated photometry from SDSS and Pan-STARRS1 as well as repeated spectra from SDSS and SDSS-III Boss, MacLeod et al. (2016) visually identify 10 changing

look quasars, with 4/10 of these objects showing emission lines broadening with at least a one magnitude increase in g-band flux and 5/10 of these objects having disappearing broad emission lines and a decreasing lightcurve (one of these five objects was discovered by LaMassa et al. 2015). One of these five objects (SDSS J1021+4645) experienced a transition from type-1 to type-1.9. MacLeod et al. (2016) report significant changes on timescales of ∼2000–3000 days with broad emission line changes corresponding to continuum changes. Variable accretion and obscuration were both
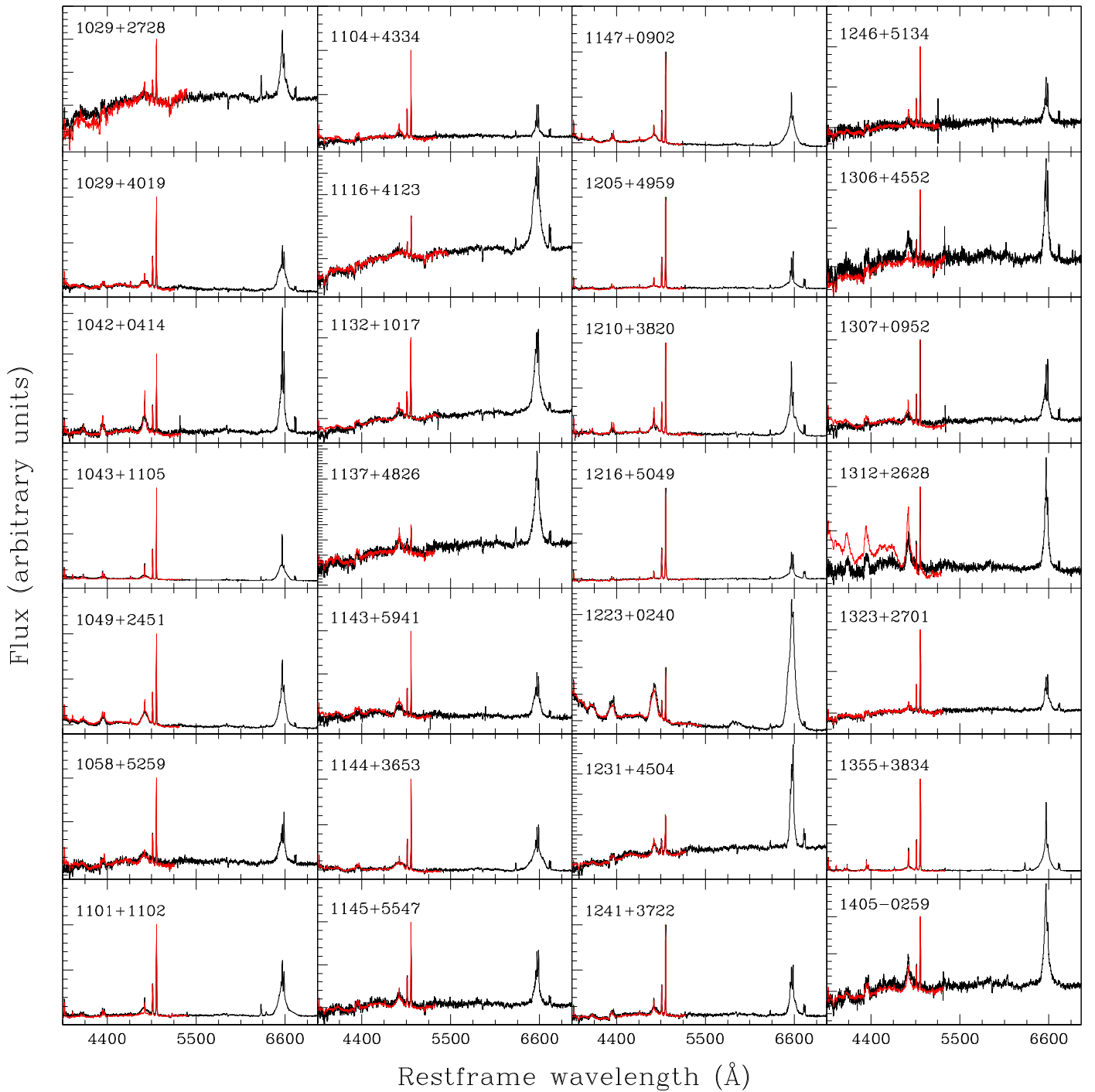
Figure 4. Same as Figure 3.

discussed as possible options to explain the observed broad-line changes, and neither possibility was ruled out (MacLeod et al. 2016). A tidal disruption flare event might explain the observed changes behind J0159+0033 (MacLeod et al. 2016; Merloni et al. 2015).

For the purpose of a reverberation mapping campaign, Barth et al. (2015) re-observed AGNs classified as Seyfert 1 galaxies based on SDSS spectra five to eight years later with the 3 m Shane telescope of Lick observatory and noted that for one object (NGC 6423), all emission lines had disappeared and that three other objects (Mrk 474, Mrk 728, and Mrk 1494) changed from Seyfert 1 to Seyfert 1.9. We will discuss

possible explanations for such extreme changes in Section 4.3.

4.2. Quantifying the Observed Broad Hβ-Line Changes

We use several measurements from our spectral decomposition of the Hβ region discussed in Section 3.2 to further quantify the observed broad Hβ line changes and explore possible origins, particularly in these four quantities: (i) the second moment of the broad Hβ component ($\sigma_{H\beta}$) from the model used to calculate M_{BH} (Bennert et al. 2011, 2015); (ii) the full width at half maximum (FWHM) of the broad Hβ line also

10
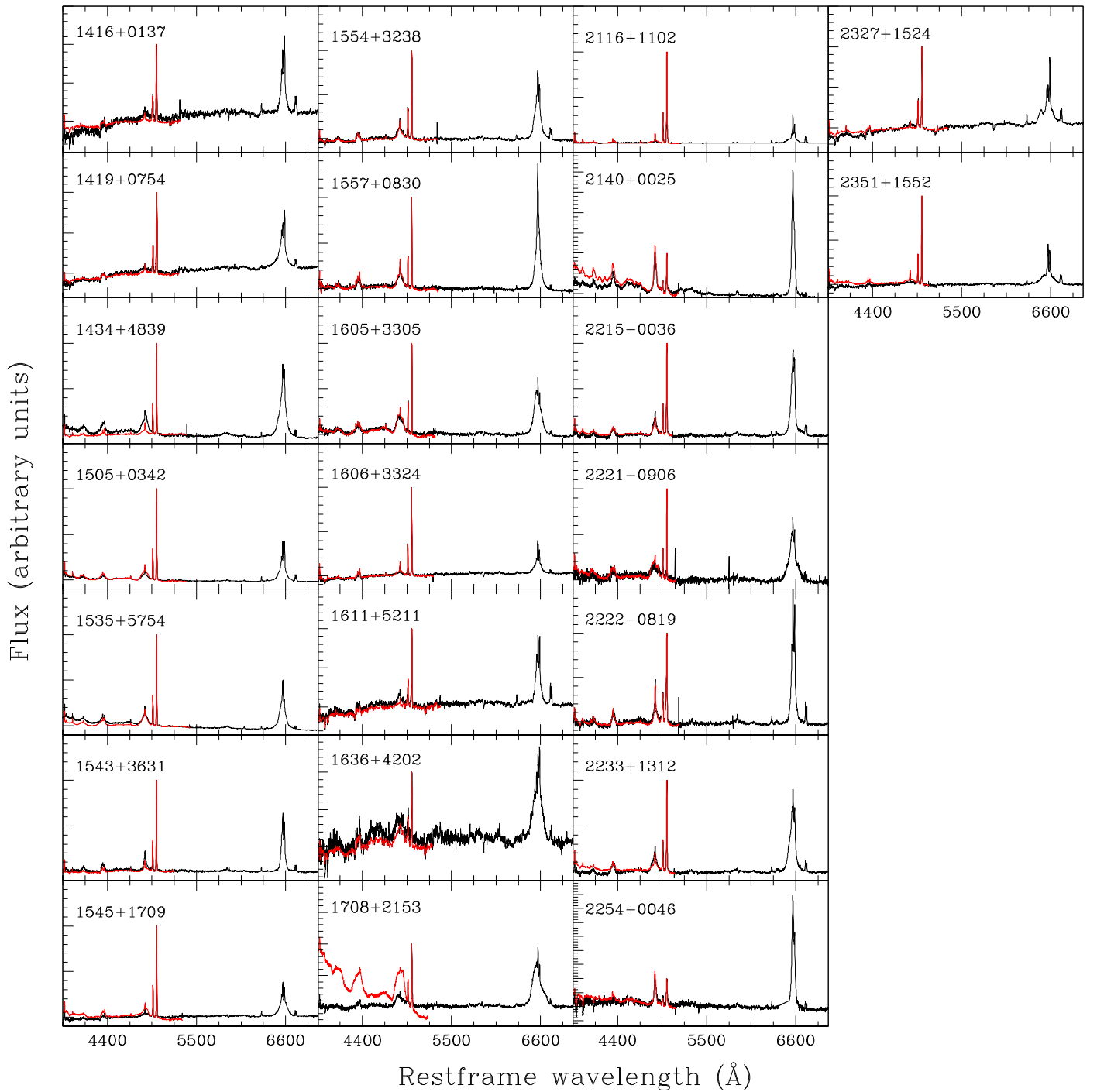
Figure 5. Same as Figure 3.

sometimes used to calculate M_{BH} (e.g., Shen et al. 2008; Shen et al. 2011)[8]; (iii) the flux ratio of the narrow Hβ component and [O III] lines, Hβ_{narrow}/[O III]; and (iv) the peak flux ratio of the broad and narrow components of the Hβ line, Hβ_{broad}/Hβ_{narrow}. In Figure 2 we compare these four quantities as derived from the SDSS spectra with those derived from the Keck spectra.

On average, the broad Hβ line is wider in the SDSS spectra than in the Keck spectra, both in $\sigma_{H\beta}$ (1.07 ± 0.29) and FWHM$_{H\beta}$ (1.08 ± 0.27) (Table 5). Moreover, the broad Hβ line has more peak flux in the SDSS spectra than in the Keck

spectra (1.26 ± 0.12). The broader and stronger Hβ line preferentially in the SDSS spectra is likely attributed to the bias in the sample selection since only objects with a broad Hβ line were chosen from SDSS.

What is noticeable in the top left panel of Figure 2 is the large scatter: for individual objects, $\sigma_{H\beta}$ can be almost up to a factor of two different between the two sets of spectra. FHWM follows a similar trend. Reverberation mapping studies have shown that the variability of the line width in AGNs correlates inversely with the variability of the power-law continuum in a way that it cancels out in the virial product, resulting in a constant M_{BH} measurement, to within $\sim$0.05 dex uncertainty

---

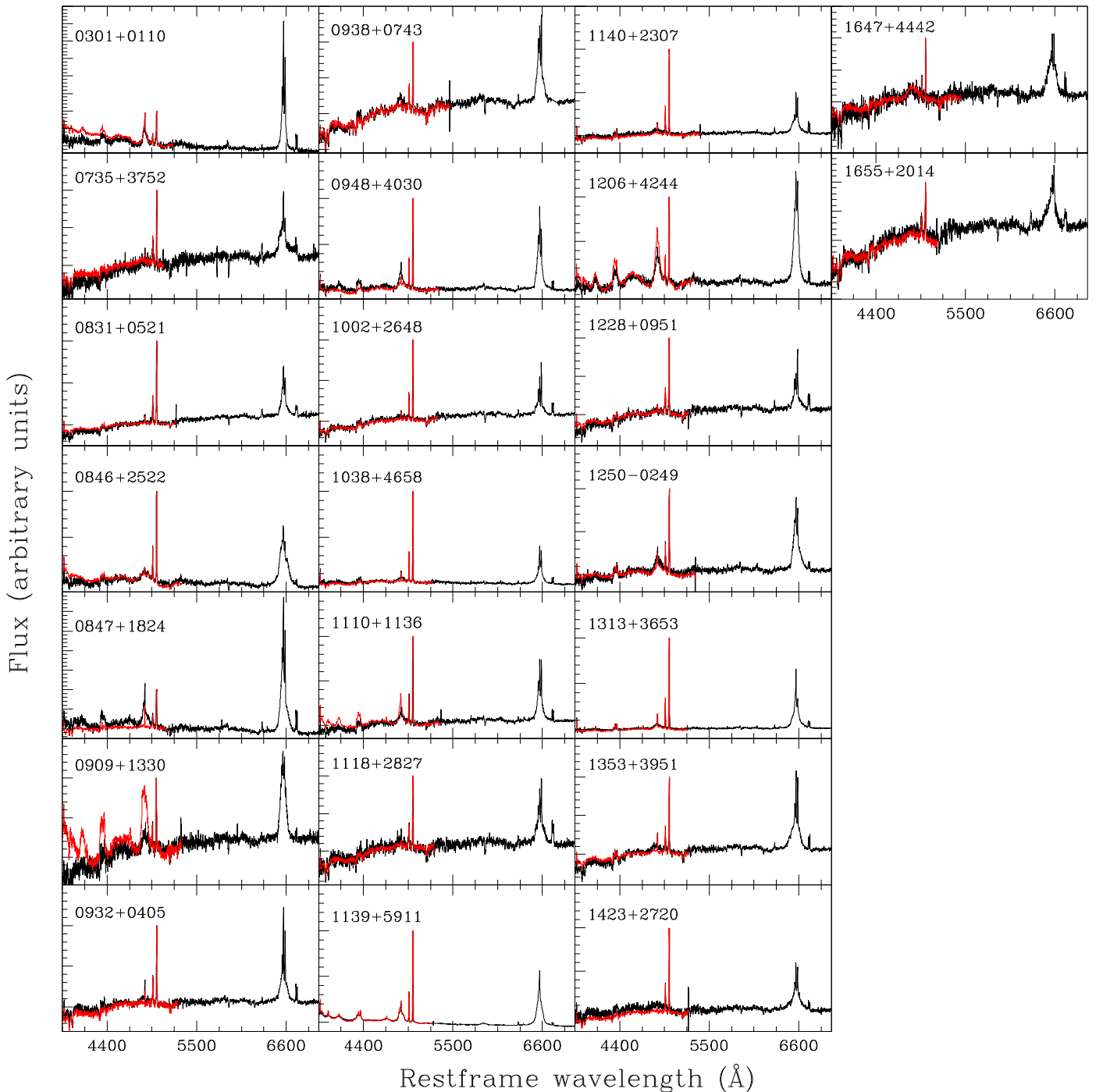[8]   For a Gaussian profile, FWHM$_{H\beta}$ = 2.35$\sigma_{H\beta}$.

Figure 6. Same as Figure 3, except that these are the 23 objects not included in Bennert et al. (2015).

(see, e.g., Bentz et al. 2007; Park et al. 2012; Barth et al. 2015). Ruan et al. (2015) also find that for their changing look quasars, the decrease in luminosity coincides with a broadening of the line widths to preserve the derived M_{BH}. Unfortunately we cannot test this correlation in this paper because we derive the host galaxy free continuum flux from a 2D image decomposition of the SDSS images (Bennert et al. 2015), taken at yet a different time from the two sets of spectra. We consider this approach superior over spectral decomposition, given unknown aperture effects for spectra. (For the same reason, image decomposition based on typically an *Hubble Space Telescope* image taken at a different

time is also used for reverberation-mapped AGNs (e.g., Bentz et al. 2013).) Moreover, the Keck spectra are not absolutely flux calibrated due to typically non-photometric observing conditions. However, using the same continuum flux derived from the 2D image decomposition, but taking into account the different width of Hβ between the SDSS and Keck spectra, the resulting M_{BH} is on average 0.05 ± 0.03 dex larger for SDSS spectra. This is small compared with the uncertainty of single-epoch measurements of 0.4 dex. Note that this includes only the 79 objects from Bennert et al. 2015, since we do not have continuum measurement for the other objects. Also, for obvious reasons,

Table 3
Results from Spectral Fitting

Object	$\sigma_{\mathrm{H}\beta}$ SDSS (km s^{-1})	FWHM$_{\mathrm{H}\beta}$ SDSS (km s^{-1})	$\frac{\mathrm{H}\beta\,\mathrm{narrow}}{[\mathrm{O\,III}]}$ Flux SDSS	$\mathrm{H}\beta\frac{\mathrm{broad}}{\mathrm{narrow}}$ Flux SDSS	$\mathrm{H}\beta\frac{\mathrm{broad}}{\mathrm{narrow}}$ Peak Flux SDSS	Fe II SDSS	$\sigma_{\mathrm{H}\beta}$ Keck (km s^{-1})	FWHM$_{\mathrm{H}\beta}$ Keck (km s^{-1})	$\frac{\mathrm{H}\beta\,\mathrm{narrow}}{[\mathrm{O\,III}]}$ Flux Keck	$\mathrm{H}\beta\frac{\mathrm{broad}}{\mathrm{narrow}}$ Flux Keck	$\mathrm{H}\beta\frac{\mathrm{broad}}{\mathrm{narrow}}$ Peak Flux Keck	Fe II Keck
(1)	(2)	(3)	(4)	(5)	(6)	(7)	(8)	(9)	(10)	(11)	(12)	(13)
0013−0951	1783 ± 135	3462 ± 205	0.13 ± 0.02	65 ± 10	8 ± 1	Y	2111 ± 211	4275 ± 594	0.17 ± 0.02	20 ± 2	2.05 ± 0.17	Y
0026+0009	964 ± 125	2276 ± 293	0.18 ± 0.05	14 ± 4	2.7 ± 0.7	N	1527 ± 227	2920 ± 765	0.26 ± 0.06	10 ± 2	1.4 ± 0.3	Y
0038+0034	2759 ± 133	7371 ± 321	0.08 ± 0.01	23.2 ± 1.8	1.54 ± 0.09	N	3328 ± 211	7223 ± 593	0.09 ± 0.01	10 ± 1	0.63 ± 0.04	Y
0109+0059	1677 ± 230	3392 ± 282	0.15 ± 0.02	4.6 ± 0.8	0.70 ± 0.09	Y	1797 ± 268	3377 ± 355	0.11 ± 0.01	4.1 ± 0.8	0.61 ± 0.06	Y
0121−0102	2070 ± 194	4069 ± 255	0.15 ± 0.03	6 ± 1	0.9 ± 0.2	Y	1742 ± 106	3145 ± 145	0.10 ± 0.01	11 ± 0.9	1.67 ± 0.09	Y
0150+0057	1799 ± 172	4816 ± 408	0.09 ± 0.01	25 ± 4	2.0 ± 0.2	N	2057 ± 129	4212 ± 242	0.07 ± 0.01	1 ± 4	3.7 ± 0.3	Y
0206−0017	2514 ± 483	5054 ± 761	0.12 ± 0.03	18 ± 5	1.68 ± 0.18	Y	1979 ± 99	4060 ± 148	0.10 ± 0.01	34 ± 3	4.7 ± 0.3	Y
0212+1406	1947 ± 198	3776 ± 299	0.11 ± 0.01	15.0 ± 1.9	1.6 ± 0.1	Y	1586 ± 129	2601 ± 242	0.15 ± 0.01	17.7 ± 1.7	2.6 ± 0.2	Y
0301+0110	2078 ± 226	3751 ± 370	0.47 ± 0.07	4.9 ± 0.8	0.90 ± 0.08	Y	1423 ± 160	3612 ± 442	0.42 ± 0.06	6.77 ± 1.08	1.16 ± 0.11	Y
0301+0115	1510 ± 182	3928 ± 181	0.05 ± 0.01	39 ± 6	6.2 ± 0.5	Y	1653 ± 105	3594 ± 200	0.09 ± 0.01	16.2 ± 1.6	2.73 ± 0.17	Y
0310−0049	1713 ± 111	3152 ± 178	0.09 ± 0.01	44 ± 6	2.9 ± 0.4	Y	1558 ± 69	2843 ± 153	0.08 ± 0.02	70 ± 12	4.9 ± 0.8	Y
0336−0706	3189 ± 177	6827 ± 416	0.19 ± 0.02	4.8 ± 0.4	0.32 ± 0.02	Y	2403 ± 164	7238 ± 552	0.16 ± 0.04	3.6 ± 1.3	0.24 ± 0.06	Y
0353−0623	1725 ± 359	4209 ± 557	0.12 ± 0.03	12 ± 4	1.0 ± 0.2	Y	1548 ± 225	3050 ± 312	0.13 ± 0.01	20 ± 4	2.12 ± 0.15	Y
0731+4522	1778 ± 107	3291 ± 260	0.18 ± 0.01	3.3 ± 0.3	0.53 ± 0.03	N	1885 ± 134	3715 ± 389	0.16 ± 0.01	4.5 ± 0.5	0.72 ± 0.04	Y
0735+3752	3120 ± 303	4572 ± 712	0.18 ± 0.06	7 ± 3	0.37 ± 0.13	Y	3996 ± 293	8070 ± 838	0.14 ± 0.06	7 ± 4	0.30 ± 0.12	N
0737+4244	1624 ± 74	4326 ± 133	0.22 ± 0.01	3.8 ± 0.2	0.41 ± 0.02	N	1692 ± 98	3361 ± 148	0.19 ± 0.01	6.2 ± 0.5	0.82 ± 0.05	Y
0802+3104	2661 ± 265	5707 ± 652	0.10 ± 0.02	34 ± 7	2.0 ± 0.4	Y	1772 ± 185	4430 ± 358	0.07 ± 0.01	19.5 ± 1.5	1.66 ± 0.11	Y
0811+1739	1779 ± 66	4325 ± 156	0.06 ± 0.01	41 ± 6	2.4 ± 0.3	Y	1520 ± 150	3520 ± 253	0.11 ± 0.02	31 ± 9	2.6 ± 0.5	Y
0813+4608	1270 ± 197	2992 ± 471	0.08 ± 0.08	5 ± 7	0.3 ± 0.3	Y	1430 ± 91	2483 ± 165	0.11 ± 0.01	14.0 ± 1.5	1.39 ± 0.11	Y
0831+0521	1040 ± 328	1197 ± 550	0.10 ± 0.02	1.3 ± 0.6	0.32 ± 0.08	N	...	...	0.11 ± 0.06	[0.06]	[0.32]	N
0845+3409	2090 ± 294	3897 ± 865	0.16 ± 0.02	9.7 ± 1.7	0.69 ± 0.07	Y	1718 ± 172	2820 ± 310	0.16 ± 0.02	7.5 ± 1.2	0.69 ± 0.08	Y
0846+2522	2572 ± 244	7398 ± 410	0.09 ± 0.02	20 ± 3	1.04 ± 0.14	Y	3394 ± 402	8304 ± 459	0.08 ± 0.02	22 ± 6	0.97 ± 0.15	Y
0847+1824	1665 ± 193	3519 ± 282	0.40 ± 0.04	8.0 ± 1.1	1.19 ± 0.08	Y	...	...	0.27 ± 0.11	[1.66]	[0.08]	N
0854+1741	2729 ± 353	4642 ± 602	0.16 ± 0.02	5.67 ± 1.08	0.84 ± 0.11	Y	1472 ± 269	2582 ± 563	0.22 ± 0.01	5 ± 1	1.36 ± 0.04	Y
0857+0528	1959 ± 193	4307 ± 282	0.17 ± 0.03	22 ± 4	1.8 ± 0.3	Y	1485 ± 120	3499 ± 51	0.1 ± 0.01	17.0 ± 1.3	1.85 ± 0.13	Y
0904+5536	2643 ± 70	5724 ± 125	0.26 ± 0.02	7.8 ± 0.4	0.48 ± 0.03	Y	2483 ± 36	7540 ± 182	0.22 ± 0.02	7.5 ± 0.5	0.45 ± 0.03	Y
0909+1330	1721 ± 251	4023 ± 416	0.12 ± 0.02	18 ± 4	2.00 ± 0.19	Y	1687 ± 138	4418 ± 148	0.19 ± 0.04	45. ± 8	4.4 ± 0.5	Y
0921+1017	2033 ± 157	4900 ± 498	0.23 ± 0.04	4.6 ± 0.9	0.31 ± 0.05	Y	2317 ± 286	4432 ± 427	0.17 ± 0.02	8.9 ± 1.4	0.71 ± 0.06	Y
0923+2254	2195 ± 254	3783 ± 545	0.51 ± 0.13	4.1 ± 0.8	0.67 ± 0.15	Y	1824 ± 265	2924 ± 668	0.24 ± 0.03	9.4 ± 2.0	1.66 ± 0.19	Y
0923+2946	2686 ± 222	5946 ± 522	0.13 ± 0.02	5.9 ± 1.1	0.24 ± 0.03	Y	2936 ± 247	5650 ± 906	0.16 ± 0.02	11.2 ± 1.7	0.56 ± 0.06	Y
0927+2301	2624 ± 226	7732 ± 647	0.10 ± 0.03	17 ± 5	1.0 ± 0.2	Y	2112 ± 205	5377 ± 367	0.08 ± 0.01	17 ± 2	1.5 ± 0.1	Y
0932+0233	2407 ± 429	6863 ± 625	0.13 ± 0.01	10 ± 2	0.50 ± 0.04	Y	1814 ± 72	4273 ± 168	0.13 ± 0.01	12.54 ± 1.04	1.05 ± 0.07	Y
0932+0405	1829 ± 75	5316 ± 427	0.26 ± 0.02	2.5 ± 0.2	0.24 ± 0.02	N	...	...	0.1 ± 0.4	[0.41]	[0]	N
0936+1014	2259 ± 153	4846 ± 228	0.09 ± 0.01	9.9 ± 0.8	1.35 ± 0.07	Y	1995 ± 80	3916 ± 123	0.10 ± 0.01	17.02 ± 1.07	2.80 ± 0.14	Y
0938+0743	1663 ± 190	4813 ± 684	0.14 ± 0.02	11 ± 2	1.04 ± 0.12	N	3723 ± 608	7110 ± 808	0.15 ± 0.12	4 ± 4	0.22 ± 0.17	N
0948+4030	1768 ± 225	3460 ± 258	0.17 ± 0.05	12 ± 4	1.2 ± 0.4	Y	3188 ± 438	6732 ± 548	0.12 ± 0.01	11.0 ± 1.8	0.57 ± 0.05	Y
1002+2648	1944 ± 184	5721 ± 433	0.12 ± 0.02	4.6 ± 1.0	0.29 ± 0.04	Y	...	...	0.12 ± 0.04	[2.23]	[0.15]	N
1029+1408	2031 ± 338	5264 ± 381	0.14 ± 0.02	9.8 ± 2.0	0.80 ± 0.08	Y	2456 ± 344	6499 ± 649	0.15 ± 0.01	8.7 ± 1.5	0.59 ± 0.05	Y
1029+2728	2103 ± 233	4958 ± 547	0.23 ± 0.06	4.1 ± 1.5	0.32 ± 0.08	Y	1544 ± 28	3634 ± 152	0.25 ± 0.03	5.07 ± 1.06	0.59 ± 0.06	Y
1029+4019	2515 ± 349	5985 ± 401	0.11 ± 0.02	8.4 ± 1.5	0.64 ± 0.07	Y	2193 ± 387	5998 ± 547	0.12 ± 0.01	6.5 ± 1.3	0.52 ± 0.04	Y
1038+4658	2621 ± 322	4750 ± 302	0.10 ± 0.01	9.4 ± 1.4	0.62 ± 0.06	Y	...	...	0.10 ± 0.14	[2.75]	[0.14]	N
1042+0414	1569 ± 194	4064 ± 166	0.34 ± 0.03	6.6 ± 1.0	0.57 ± 0.04	Y	1518 ± 102	2724 ± 145	0.33 ± 0.03	5.6 ± 0.6	0.73 ± 0.05	Y
1043+1105	2864 ± 149	6171 ± 230	0.21 ± 0.04	10.5 ± 1.7	0.61 ± 0.06	Y	2313 ± 28	6597 ± 152	0.13 ± 0.01	4.7 ± 0.2	0.25 ± 0.02	Y
1049+2451	2368 ± 161	5181 ± 207	0.15 ± 0.03	14.2 ± 1.8	0.97 ± 0.14	Y	2534 ± 135	5112 ± 203	0.15 ± 0.01	15.1 ± 1.2	1.04 ± 0.07	Y

Table 3
(Continued)

Object	$\sigma_{H\beta}$ SDSS (km s^{-1})	FWHM$_{H\beta}$ SDSS (km s^{-1})	$\frac{H\beta \text{narrow}}{[\text{O III}]}$ Flux SDSS	$H\beta\frac{\text{broad}}{\text{narrow}}$ Flux SDSS	$H\beta\frac{\text{broad}}{\text{narrow}}$ Peak Flux SDSS	Fe II SDSS	$\sigma_{H\beta}$ Keck (km s^{-1})	FWHM$_{H\beta}$ Keck (km s^{-1})	$\frac{H\beta \text{narrow}}{[\text{O III}]}$ Flux Keck	$H\beta\frac{\text{broad}}{\text{narrow}}$ Flux Keck	$H\beta\frac{\text{broad}}{\text{narrow}}$ Peak Flux Keck	Fe II Keck
(1)	(2)	(3)	(4)	(5)	(6)	(7)	(8)	(9)	(10)	(11)	(12)	(13)
1058+5259	1987 ± 400	4928 ± 940	0.07 ± 0.01	18 ± 5	1.24 ± 0.18	N	1896 ± 150	5372 ± 150	0.10 ± 0.01	13.3 ± 1.7	0.92 ± 0.08	Y
1101+1102	2558 ± 125	6047 ± 295	0.14 ± 0.03	7.6 ± 1.2	0.62 ± 0.13	N	3949 ± 170	8349 ± 597	0.13 ± 0.01	3.5 ± 0.3	0.20 ± 0.01	Y
1104+4334	1873 ± 308	4319 ± 647	0.09 ± 0.02	4.4 ± 1.3	0.31 ± 0.06	Y	1719 ± 160	4072 ± 395	0.12 ± 0.01	9.4 ± 1.2	0.84 ± 0.07	Y
1110+1136	1878 ± 206	3860 ± 400	0.14 ± 0.01	10.4 ± 1.6	0.78 ± 0.05	Y	1378 ± 95	2898 ± 150	0.15 ± 0.01	14.7 ± 1.5	1.68 ± 0.12	Y
1116+4123	2531 ± 294	6324 ± 692	0.25 ± 0.04	10.2 ± 1.9	0.56 ± 0.07	N	3136 ± 315	6774 ± 740	0.27 ± 0.04	6.6 ± 1.3	0.39 ± 0.05	Y
1118+2827	1908 ± 136	5910 ± 498	0.21 ± 0.03	3.8 ± 0.7	0.38 ± 0.05	N	...	...	0.14 ± 0.05	[2.05]	[0.19]	N
1132+1017	2028 ± 147	5782 ± 345	0.10 ± 0.01	7.7 ± 1.3	0.74 ± 0.09	Y	1900 ± 86	5341 ± 740	0.09 ± 0.01	15.8 ± 1.4	1.63 ± 0.11	Y
1137+4826	1750 ± 357	3663 ± 647	0.34 ± 0.05	5.8 ± 1.4	0.94 ± 0.14	Y	1606 ± 92	3788 ± 222	0.45 ± 0.06	6.8 ± 0.9	1.00 ± 0.09	Y
1139+5911	2333 ± 158	4262 ± 218	0.16 ± 0.06	20 ± 4	2.2 ± 0.7	Y	2228 ± 111	3994 ± 221	0.09 ± 0.01	22.2 ± 1.7	1.73 ± 0.11	Y
1140+2307	2710 ± 235	5014 ± 668	0.10 ± 0.01	8.0 ± 1.2	0.43 ± 0.05	N	3324 ± 330	6376 ± 586	0.12 ± 0.01	4.4 ± 0.6	0.24 ± 0.02	N
1143+5941	2002 ± 446	5629 ± 863	0.13 ± 0.04	15.0 ± 2.7	0.77 ± 0.18	Y	1790 ± 128	5405 ± 424	0.08 ± 0.01	38 ± 4	2.00 ± 0.08	Y
1144+3653	3016 ± 292	8301 ± 579	0.08 ± 0.01	21 ± 3	0.90 ± 0.14	N	2933 ± 205	8009 ± 145	0.08 ± 0.01	16.3 ± 1.5	0.87 ± 0.05	N
1145+5547	2078 ± 422	4298 ± 611	0.10 ± 0.01	14 ± 3	1.18 ± 0.12	Y	1837 ± 208	4465 ± 391	0.15 ± 0.01	7.49 ± 1.06	0.71 ± 0.05	Y
1147+0902	3733 ± 226	6475 ± 563	0.14 ± 0.05	13 ± 3	0.9 ± 0.3	N	2896 ± 188	5285 ± 543	0.12 ± 0.01	10.9 ± 1.2	0.73 ± 0.06	Y
1205+4959	3572 ± 201	8275 ± 650	0.11 ± 0.02	3.9 ± 0.4	0.24 ± 0.03	Y	2678 ± 294	5552 ± 374	0.10 ± 0.01	3.6 ± 0.5	0.31 ± 0.02	Y
1206+4244	1925 ± 167	3889 ± 211	0.15 ± 0.02	24 ± 3	2.4 ± 0.3	Y	1614 ± 92	3800 ± 144	0.17 ± 0.02	36 ± 3	3.6 ± 0.3	Y
1210+3820	2499 ± 432	6413 ± 513	0.20 ± 0.04	5.9 ± 1.5	0.36 ± 0.06	N	2831 ± 148	5300 ± 392	0.20 ± 0.02	8.0 ± 0.7	0.58 ± 0.04	Y
1216+5049	3329 ± 180	8923 ± 422	0.11 ± 0.02	2.3 ± 0.3	0.19 ± 0.03	Y	4487 ± 477	7810 ± 392	0.09 ± 0.01	2.1 ± 0.3	0.15 ± 0.01	Y
1223+0240	2780 ± 160	5802 ± 220	0.05 ± 0.02	207 ± 44	17 ± 6	Y	2306 ± 107	5051 ± 168	0.10 ± 0.01	69 ± 6	5.7 ± 0.4	Y
1228+0951	2289 ± 657	7303 ± 1543	0.12 ± 0.07	3 ± 3	0.23 ± 0.14	Y	2331 ± 456	6011 ± 495	0.12 ± 0.04	3.2 ± 1.6	0.28 ± 0.10	Y
1231+4504	1551 ± 343	2872 ± 440	0.20 ± 0.03	5.5 ± 1.4	1.27 ± 0.14	Y	1555 ± 168	3325 ± 394	0.16 ± 0.02	9.1 ± 1.2	1.91 ± 0.16	Y
1241+3722	1829 ± 93	4320 ± 219	0.13 ± 0.02	7.9 ± 0.9	0.69 ± 0.08	N	1574 ± 100	3185 ± 197	0.11 ± 0.01	6.0 ± 0.8	0.70 ± 0.07	Y
1246+5134	2402 ± 313	4403 ± 703	0.07 ± 0.05	10 ± 11	0.6 ± 0.5	Y	1141 ± 130	2270 ± 185	0.09 ± 0.01	12.0 ± 1.8	1.52 ± 0.12	Y
1250−0249	2068 ± 323	5304 ± 732	0.17 ± 0.03	9 ± 2	0.89 ± 0.13	Y	2417 ± 246	5771 ± 541	0.18 ± 0.01	7.3 ± 0.9	0.61 ± 0.04	Y
1306+4552	1327 ± 148	3262 ± 237	0.15 ± 0.02	18 ± 3	1.9 ± 0.2	N	1892 ± 297	4129 ± 772	0.22 ± 0.04	2.8 ± 0.8	0.27 ± 0.05	Y
1307+0952	1616 ± 114	3748 ± 267	0.09 ± 0.04	11 ± 7	0.8 ± 0.3	N	1630 ± 165	3586 ± 249	0.14 ± 0.01	12.7 ± 1.7	1.10 ± 0.09	N
1312+2628	1585 ± 171	3131 ± 256	0.12 ± 0.03	32 ± 10	2.8 ± 0.5	Y	1572 ± 150	2924 ± 345	0.22 ± 0.03	36 ± 6	2.95 ± 0.17	Y
1313+3653	2592 ± 217	5591 ± 402	0.14 ± 0.02	4.8 ± 0.5	0.34 ± 0.03	Y	2115 ± 264	4920 ± 347	0.13 ± 0.01	4.2 ± 0.6	0.34 ± 0.02	Y
1323+2701	4266 ± 349	10123 ± 299	0.089 ± 0.004	18.3 ± 1.7	0.79 ± 0.02	Y	2414 ± 376	5219 ± 782	0.10 ± 0.01	5.9 ± 1.2	0.54 ± 0.06	Y
1353+3951	2037 ± 121	6308 ± 537	0.19 ± 0.02	4.1 ± 0.5	0.31 ± 0.02	N	...	...	0.2 ± 0.7	[1.52]	[0.31]	N
1355+3834	2842 ± 79	5936 ± 245	0.28 ± 0.05	3.3 ± 0.3	0.36 ± 0.06	Y	4034 ± 301	6371 ± 277	0.20 ± 0.02	3.2 ± 0.3	0.22 ± 0.01	N
1405−0259	1873 ± 212	3518 ± 549	0.21 ± 0.02	13 ± 2	1.48 ± 0.13	Y	1599 ± 140	2933 ± 260	0.16 ± 0.02	11.1 ± 1.4	1.48 ± 0.12	Y
1416+0317	11853 ± 251	4022 ± 589	0.12 ± 0.02	5.4 ± 1.1	0.78 ± 0.09	Y	1514 ± 233	3565 ± 550	0.11 ± 0.02	2.2 ± 0.5	0.40 ± 0.05	Y
1419+0754	1940 ± 154	5517 ± 362	0.10 ± 0.02	2.9 ± 0.7	0.35 ± 0.06	N	3006 ± 371	5780 ± 529	0.10 ± 0.01	3.5 ± 1.0	0.36 ± 0.07	Y
1423+2720	3428 ± 264	7873 ± 621	0.11 ± 0.03	12 ± 4	0.5 ± 0.1	Y	...	...	0.08 ± 0.04	[2.45]	[0]	Y
1434+4839	2268 ± 171	4351 ± 534	0.08 ± 0.02	35 ± 7	2.7 ± 0.6	Y	1731 ± 85	4475 ± 222	0.09 ± 0.01	6.0 ± 0.4	0.58 ± 0.03	Y
1505+0342	2280 ± 215	5028 ± 569	0.14 ± 0.03	6.9 ± 1.3	0.83 ± 0.12	N	1956 ± 139	5782 ± 154	0.08 ± 0.01	17.8 ± 1.6	1.55 ± 0.09	Y
1535+5754	2431 ± 311	4191 ± 565	0.09 ± 0.03	16 ± 5	1.4 ± 0.4	Y	2442 ± 93	5088 ± 127	0.08 ± 0.01	16.2 ± 1.3	1.41 ± 0.07	Y
1543+3631	1527 ± 171	2849 ± 197	0.14 ± 0.02	7.1 ± 1.1	1.03 ± 0.15	Y	1820 ± 168	3831 ± 248	0.09 ± 0.01	4.0 ± 0.5	0.47 ± 0.03	Y
1545+1709	2158 ± 156	5555 ± 275	0.09 ± 0.01	6.5 ± 0.6	0.52 ± 0.05	N	3588 ± 226	4612 ± 237	0.06 ± 0.01	24 ± 3	1.68 ± 0.14	N
1554+3238	2067 ± 104	4887 ± 246	0.14 ± 0.02	7.2 ± 0.8	0.83 ± 0.11	N	2523 ± 159	4148 ± 258	0.11 ± 0.01	7.9 ± 0.7	1.04 ± 0.06	Y
1557+0830	13174 ± 214	5054 ± 185	0.18 ± 0.03	11.9 ± 1.5	0.87 ± 0.09	Y	2388 ± 91	4817 ± 156	0.17 ± 0.02	15.1 ± 1.4	1.09 ± 0.08	Y
1605+3305	2153 ± 101	5079 ± 230	0.06 ± 0.02	54 ± 13	2.9 ± 1.0	Y	1960 ± 272	5302 ± 637	0.10 ± 0.01	33 ± 5	2.03 ± 0.14	Y
1606+3324	2158 ± 170	5087 ± 393	0.10 ± 0.01	3.8 ± 0.5	0.34 ± 0.04	N	2053 ± 80	5088 ± 739	0.12 ± 0.01	4.4 ± 0.3	0.45 ± 0.03	Y

Table 3
(Continued)

Object	$\sigma_{H\beta}$ SDSS (km s^{-1})	FWHM$_{H\beta}$ SDSS (km s^{-1})	$\frac{H\beta narrow}{[O\,III]}$ Flux SDSS	$H\beta\frac{broad}{narrow}$ Flux SDSS	$H\beta\frac{broad}{narrow}$ Peak Flux SDSS	Fe II SDSS	$\sigma_{H\beta}$ Keck (km s^{-1})	FWHM$_{H\beta}$ Keck (km s^{-1})	$\frac{H\beta narrow}{[O\,III]}$ Flux Keck	$H\beta\frac{broad}{narrow}$ Flux Keck	$H\beta\frac{broad}{narrow}$ Peak Flux Keck	Fe II Keck
(1)	(2)	(3)	(4)	(5)	(6)	(7)	(8)	(9)	(10)	(11)	(12)	(13)
1611+5211	1392 ± 207	3895 ± 486	0.16 ± 0.03	4.8 ± 1.1	0.71 ± 0.10	N	2515 ± 410	7695 ± 964	0.12 ± 0.03	2.9 ± 1.1	0.27 ± 0.07	Y
1636+4202	2367 ± 223	6655 ± 621	0.07 ± 0.01	39 ± 7	3.7 ± 0.4	Y	2492 ± 230	4542 ± 523	0.10 ± 0.01	24 ± 3	2.45 ± 0.19	Y
1647+4442	2227 ± 279	6228 ± 655	0.09 ± 0.02	4.8 ± 1.9	1.3 ± 0.4	N	2921 ± 246	8325 ± 214	0.20 ± 0.03	21 ± 4	0.77 ± 0.08	N
1655+2014	⋯	⋯	⋯	⋯	⋯	N	⋯	⋯	⋯	⋯	⋯	N
1708+2153	2829 ± 134	6055 ± 580	0.11 ± 0.01	15.2 ± 1.2	1.49 ± 0.08	Y	2402 ± 122	7359 ± 245	0.13 ± 0.02	62 ± 10	6.2 ± 0.6	Y
2116+1102	2790 ± 27	6577 ± 64	0.0903 ± 0.0002	2.25 ± 0.02	0.1831 ± 0.0003	Y	2484 ± 42	7186 ± 248	0.084 ± 0.005	3.63 ± 0.18	0.33 ± 0.01	Y
2140+0025	1329 ± 104	2225 ± 127	0.53 ± 0.09	7.1 ± 1.1	1.47 ± 0.12	Y	1114 ± 64	2155 ± 127	0.29 ± 0.04	17 ± 2	3.7 ± 0.4	Y
2215−0036	1877 ± 200	3330 ± 155	0.12 ± 0.01	8.5 ± 1.1	1.58 ± 0.14	Y	1636 ± 92	3966 ± 220	0.09 ± 0.01	7.3 ± 0.6	1.14 ± 0.06	Y
2221−0906	2498 ± 394	6684 ± 539	0.10 ± 0.01	21 ± 4	1.20 ± 0.10	N	2375 ± 131	6012 ± 224	0.12 ± 0.01	24 ± 2	1.45 ± 0.11	Y
2222−0819	1811 ± 88	3327 ± 319	0.25 ± 0.02	2.5 ± 0.2	0.55 ± 0.03	N	1799 ± 168	2861 ± 343	0.2 ± 0.02	2.5 ± 0.3	0.66 ± 0.03	Y
2233+1312	1897 ± 66	4409 ± 236	0.19 ± 0.02	6.7 ± 0.4	0.90 ± 0.06	N	2477 ± 135	5830 ± 318	0.16 ± 0.01	5.7 ± 0.5	0.53 ± 0.04	N
2254+0046	1466 ± 200	2015 ± 195	0.56 ± 0.09	3.9 ± 0.8	1.26 ± 0.17	Y	859 ± 194	1398 ± 286	0.59 ± 0.07	4.7 ± 1.1	1.66 ± 0.18	Y
2327+1524	3267 ± 206	4098 ± 707	0.06 ± 0.01	11.0 ± 1.6	1.10 ± 0.13	N	1924 ± 166	5807 ± 390	0.08 ± 0.02	2.0 ± 0.7	0.22 ± 0.06	N
2351+1552	3533 ± 269	10437 ± 526	0.12 ± 0.01	3.6 ± 0.4	0.20 ± 0.02	N	2974 ± 144	7803 ± 394	0.11 ± 0.01	6.7 ± 0.6	0.43 ± 0.03	N

Note. Column (1): target ID based on R.A. and decl. used throughout the text. Column (2): second moment of broad Hβ from SDSS spectrum (in km s^{-1}). Column (3): FWHM of broad Hβ from SDSS spectrum (in km s^{-1}). Column (4): integrated flux ratio of Hβ/[O III] from SDSS spectrum. Column (5): integrated flux ratio of Hβ broad/narrow from SDSS spectrum. Column (6): peak flux ratio of Hβ broad/narrow from SDSS spectrum. Column (7): whether Fe II was subtracted from the SDSS spectrum during the fitting process. Column (8): second moment of broad Hβ from Keck spectrum (in km s^{-1}). Column (9): FWHM of broad Hβ from Keck spectrum (in km s^{-1}). Column (10): integrated flux ratio of Hβ/[O III] from Keck spectrum. Column (11): integrated flux ratio of Hβ broad/narrow from Keck spectrum. Column (12): peak flux ratio of Hβ broad/narrow from Keck spectrum. Column (13): whether Fe II was subtracted from the Keck spectrum during the fitting process. Note that the values in brackets are estimated from upper limits on the broad Hβ flux for objects classified as Sy 1.9 or Sy 2, that is without an obvious broad Hβ component. No width (FWHM or σ) of broad Hβ is given in those cases. Also note that for object 1655+2014 the S/N was too low in both SDSS and Keck spectra to produce a reliable fit to the Hβ region. No values are given for this object and it is not included in the quantitative analysis.
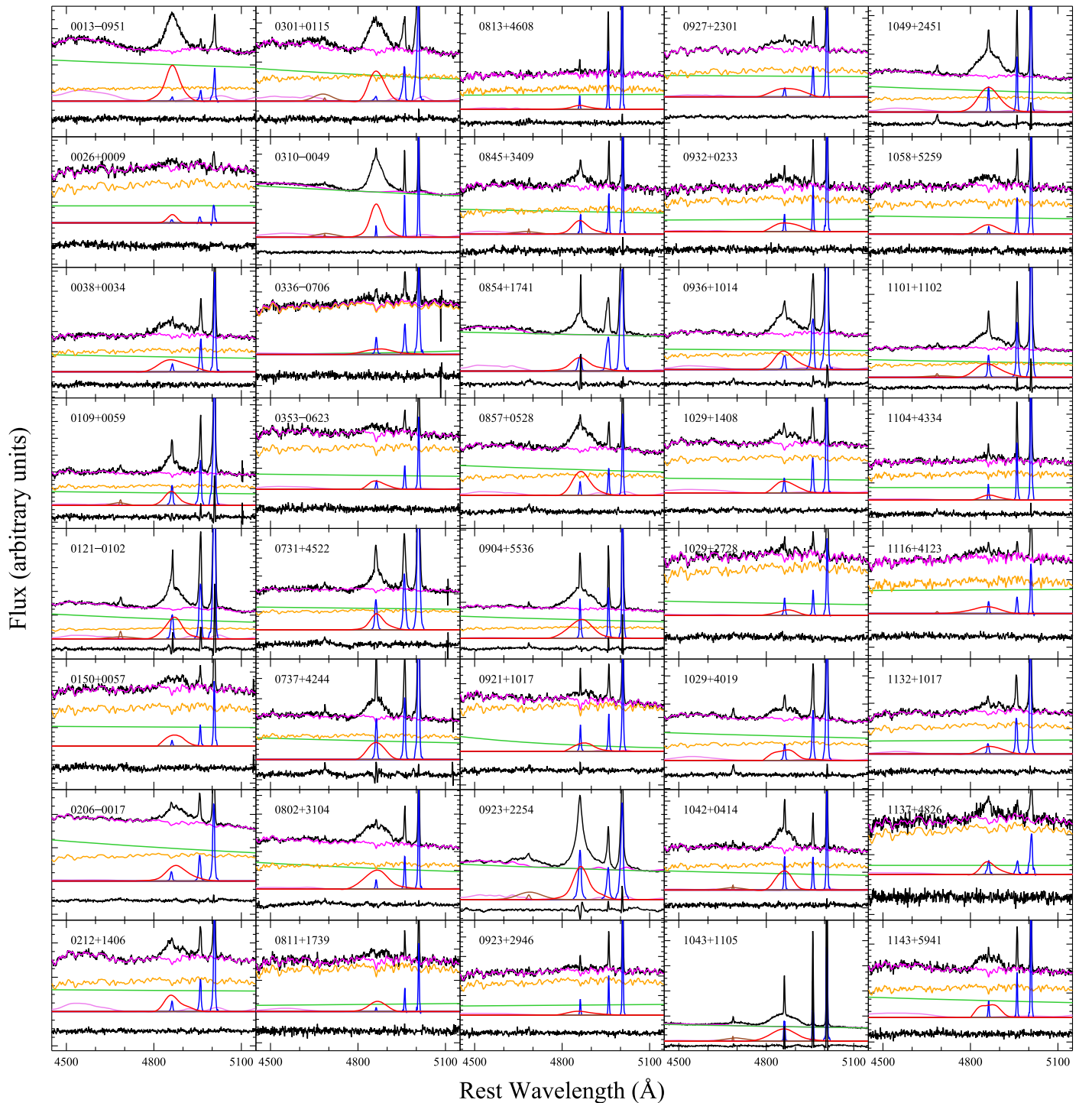
Figure 7. Multi-component spectral decomposition of the Hβ region in SDSS spectra. In the upper region, the observed spectrum is shown in black with the best fit of the continuum, Fe ɪɪ, and host galaxy starlight in magenta. Below that the best fit to the power-law continuum is shown in green with the stellar spectrum in yellow. Below this the narrow lines of Hβ λ4861, and [O ɪɪɪ] λλ4959, 5007 are shown in blue, the broad and narrow components of He ɪɪ λ4686 in brown, and the broad component of Hβ in red. The residuals are plotted in black (arbitrarily shifted downward for clarity). Note that the objects shown here are included in Bennert et al. (2015), who show the corresponding fit to the Keck spectra in their Figure 3.

it excludes any object without broad Hβ emission in the Keck spectra.

The lower left panel of Figure 2 shows that while overall the $H\beta_{narrow}$/[O ɪɪɪ] flux ratio as measured in the SDSS spectra is comparable to that in the Keck spectra (on average 1.04 ± 0.32) with the majority of the objects falling near the unity line, the scatter is large due to some extreme outliers. While the large scatter could partially be due to the change in

broad Hβ (as a consequence of the observed Seyfert-type change) effecting the narrow Hβ flux for fitting reasons since the lines are blended, we consider such an effect negligible given the quality of our data and our fitting procedure. More likely it might indicate that the NLR emission lines are not constant over the timescales of these observations but do indeed reverberate, which is in line with recent studies by (Peterson et al. 2013; Barth et al. 2015).
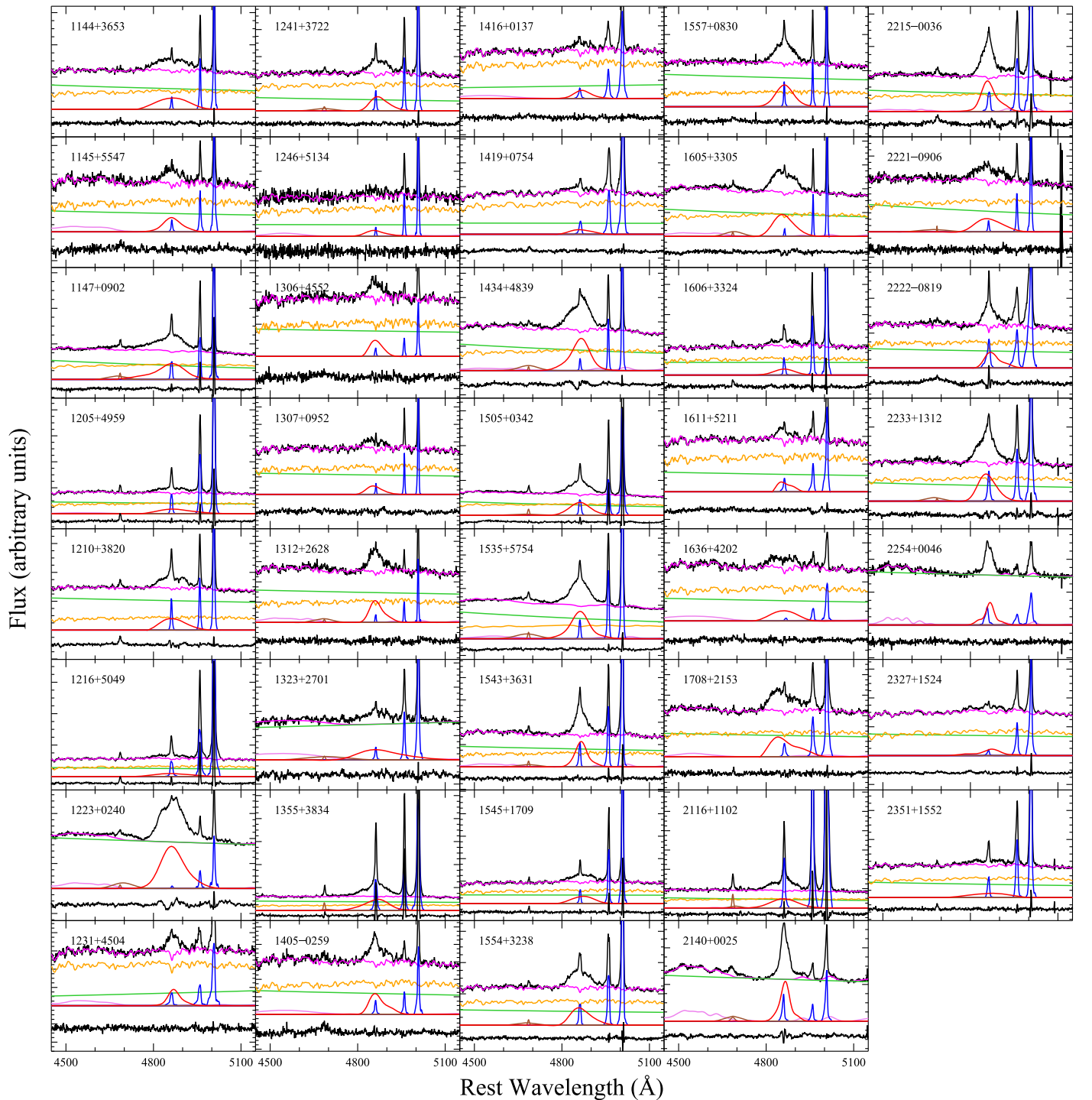
Figure 8. Same as Figure 7.

In the lower right panel of Figure 2, the broad Hβ to narrow Hβ peak flux ratio varies quite a bit between SDSS and Keck spectra (1.26 ± 0.12). This reflects the change in the broad Hβ emission line, and as a consequence, Seyfert type. On average, the broad Hβ line is stronger in the SDSS spectra than in the Keck spectra, most likely due the selection bias. The change in peak flux ratio can be used as an independent way to classify Seyfert-type transitions, as discussed in Section 4.1.

Reverberation mapping studies have revealed an anti-correlation between broad Hβ width and luminosity (Denney et al. 2009; Park et al. 2012; Barth et al. 2015), which is attributed to the relation between ionizing flux and the local reprocessing efficiency of the BLR gas: the Hβ reprocessing efficiency is greatest in the outer part of the BLR where the flux from the continuum is lower (Korista & Goad 2004; Goad & Korista 2014). Therefore, higher levels of continuum luminosity lead to an increase in emissivity-weighted BLR radius. This
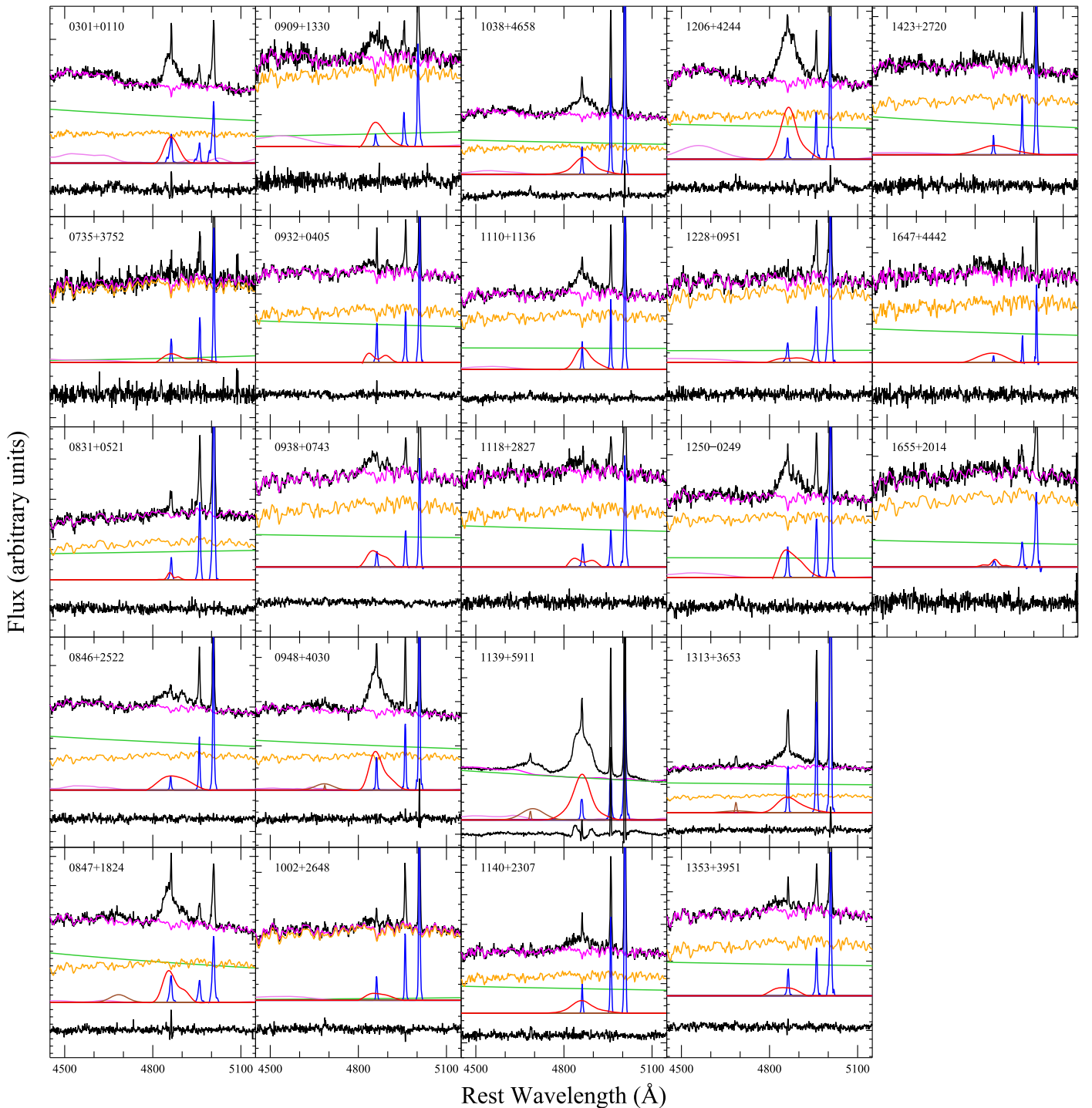
Figure 9. Same as Figure 7, but for 23 objects not included in Bennert et al. (2015).

so-called breathing effect increases flux for low-velocity line core relative to high-velocity wings, which makes the line profile narrower. BLR breathing occurs on short timescales of days to weeks in response to AGN continuum variations. However, our data do not generally support this special kind of line variability.

Variable accretion and/or variable obscuration are considered the two main causes for a type change. As discussed above, to

distinguish between them, the variability in X-ray, UV, and optical is typically studied. However, we do not have X-ray data concurring with the SDSS and Keck spectra. Figures 3–6 show a qualitative comparison between the change in Hβ and power-law, overlaying the unsubtracted spectra of SDSS and Keck for each object, scaled to [O III]. There are 41/102 (~40%) objects that have a stronger power-law emission in Keck than in SDSS; for 17/102 (~17%) it is the other way around, and 44/102
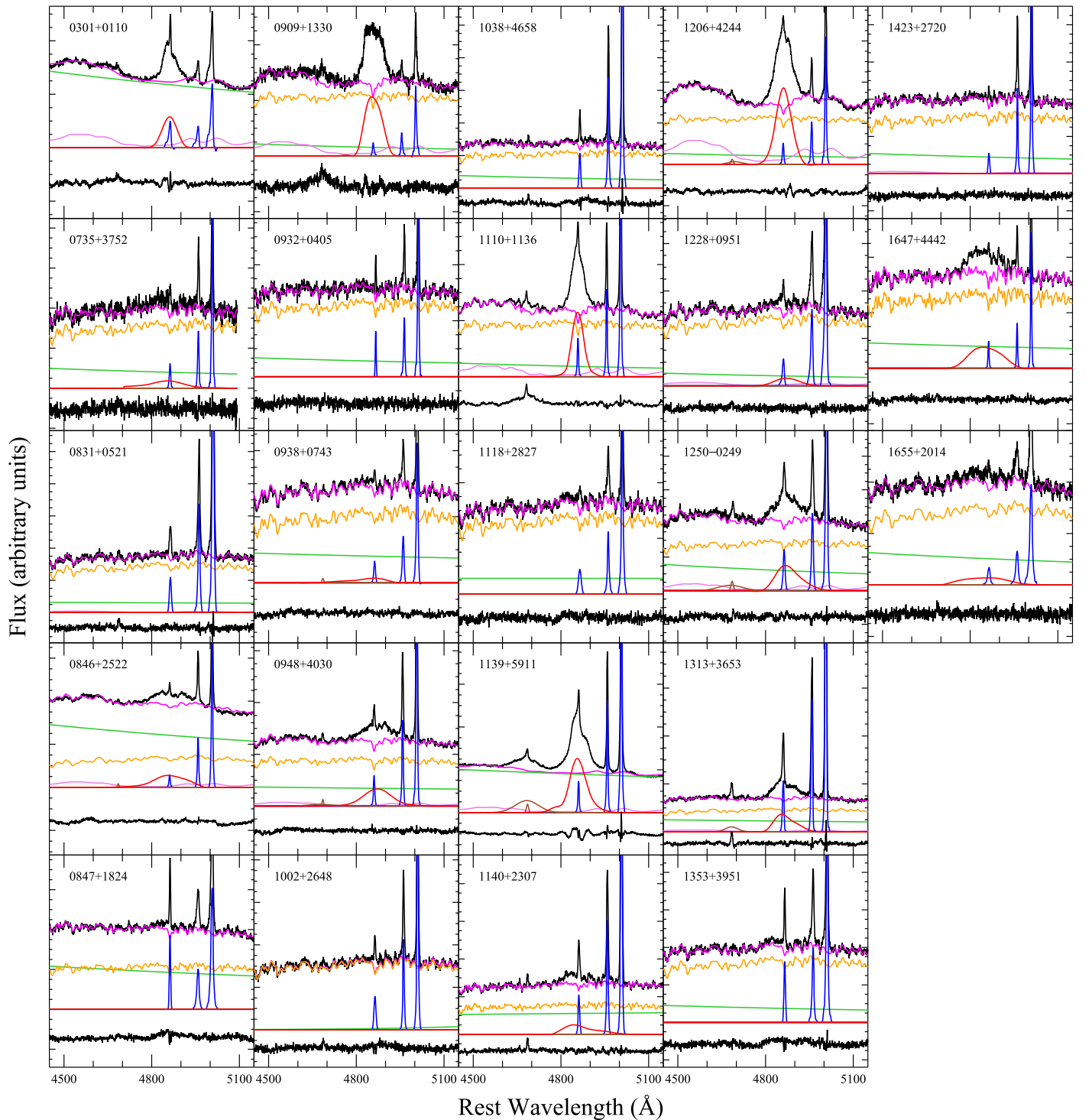
Figure 10. Same as Figure 9 for spectra gathered from Keck and not included in Bennert et al. (2015).

(∼43%) show no notable change. The higher fraction of non-stellar (power-law) continuum in the Keck spectra is explainable by the smaller slit and sharper seeing.

In other words, both the broad Hβ emission line as well as the power-law continuum vary between the two set of spectra. However, when attempting to quantify those changes, we do not find them to be directly correlated. This is not too surprising, since any variation between broad Hβ emission and power-law continuum are offset in time depending on the time-

lag of a given object and would not show up at the same time in a single-epoch spectrum (see e.g., Figures 7 and 8 in Park et al. 2012).

Aperture effects may play a role in our results: Keck spectra (1″ × 1″ square), given the seeing, only include the unresolved emission from BLR, AGN power-law continuum, and NLR, while the SDSS spectra (1″.5 radius circular fiber) may additionally include more extended NLR flux. However, any aperture effect would artificially boost the ratio of broad-to-
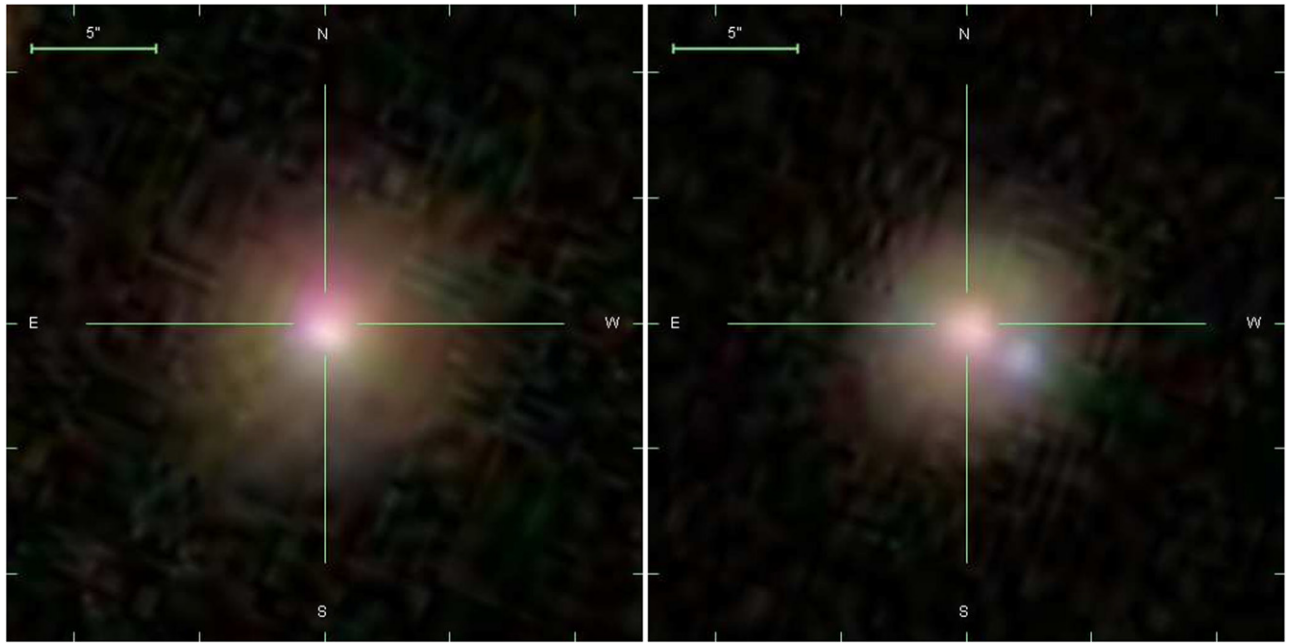
Figure 11. SDSS multi-color image for 0847+1824 (left) taken on 2004 December 13, roughly a year before the SDSS spectrum, and 1038+4658 (right) taken on 2002 February 08, roughly 10 months before the SDSS spectrum. For 0847+1824, there is extended emission offset $\sim 1''$ to the northeast of the galaxy center. For 1038+4658, an emission blob can be seen $\sim 2''.5$ to the southwest of the galaxy center. In both cases, the extended emission might have been missed in the Keck spectra due to the smaller width longslit (with a position angle not covering the emission), but included in the $3''$ fiber of SDSS.

Table 4
Extreme Seyfert-type Changes

Object	Class. SDSS	Class. Keck	Class. Lick	Notes
(1)	(2)	(3)	(4)	(5)
0847+1824	1	1.9	2	Off-centered emission in the SDSS image
				Type-1 also in the literature spectrum taken ~ 1.8 years before SDSS
1038+4658	1.5	1.9	1.9	Off-centered blob in the SDSS image
1423+2720	1.5	1.9	1.8	Low S/N in the SDSS spectrum

Note. Column (1): Object (for more details see Table 2). Column (2): Seyfert-type classification based on SDSS spectrum. Column (3): Seyfert-type classification based on Keck spectrum. Column (4): Seyfert-type classification based on Lick spectrum. Column (5): Notes (see the text for further discussion).

Table 5
Comparison between SDSS and Keck

Data	Average
(1)	(2)
$\sigma_{H\beta}$	1.07 ± 0.03
$FHWM_{H\beta}$	1.08 ± 0.03
$H\beta_{narrow}/[O\ III]$	1.04 ± 0.03
$H\beta_{broad}/H\beta_{narrow}$	1.26 ± 0.12

Note. Column (1): comparison between values derived from the SDSS spectra vs. those derived from the Keck spectra for quantities listed in this column. Column (2): average and scatter.

narrow flux in Keck spectra (both peak and integrated) compared with SDSS spectra, since Keck spectra are restricted to a smaller central area and thus focus on the unresolved emission. Thus, aperture effects cannot explain the opposite trend that we are observing in the majority of objects, namely that we observe less broad $H\beta$ in the Keck spectra.

We note that a few objects (e.g., 0909+1330, 1312+2628, 1708+2153, and 2140+0025) show significantly stronger blue continuum emission (Figures 3–6). This rise in the blue wavelength range cannot simply be explained by the fact that the Keck spectra were not obtained at parallactic angle since this would have the opposite effect. Similarly, none of the SDSS spectra were taken at large airmasses with the exception of 2140+0025, observed at an airmass of 1.3, which could have reduced the blue wavelengths emission artificially for that object in the SDSS spectrum. To further test whether the rise in the blue wavelengths emission in the Keck spectra compared to SDSS is an artifact of Keck flux calibration, we looked at the spatially resolved spectra. The rise in the blue continuum is only present in the central spectra within the seeing limits but not in the outer spectra, suggesting that it is a real trend. A stronger power-law continuum may indeed explain the Seyfert-type change observed for 0909+1330 (from 1.8 in SDSS to 1 in Keck) and 1708+2153 (from 1.5 in SDSS to 1 in Keck). (Note that the other two objects were classified as Seyfert 1 in

both spectra). However, as mentioned above, part of this higher fraction of power-law continuum in the Keck spectra can simply be due to the smaller aperture and sharper seeing compared with SDSS.

4.3. Extreme Seyfert-type Changes

For three objects in the sample, the broad Hβ component was very prominent in the SDSS spectra, but decreased significantly and virtually disappeared in the Keck spectra. All three were re-observed with the 3 m Shane telescope of Lick observatory (Scott 2013). Table 4 summarizes the Seyfert-type changes of these objects. Note that all Keck objects classified conservatively as type-1.9 could be a type-2 object; however, the spectra do not extend to Hα, so we cannot distinguish between the two. Especially in those cases where the Lick spectrum reveals a type-2 object, it is likely that the object was also a type-2 in the Keck spectrum. Also note that for 1423 +2720 the SDSS spectrum has a low S/N, making it difficult to model the underlying broad Hβ line.

The continuum luminosity at 5100 Å was compared for all objects in the sample in order to determine if there was a correlation between AGN luminosity and strongly variable objects, but no correlation was found.

For all objects, we carefully searched the literature for other optical spectra. 0847+1824 is the only object for which this search was successful: it was previously observed on 02-28-2004 (MJD 53063) before the SDSS observation, and from that spectrum the AGN was a type-1 Seyfert (Ho & Kim 2009).

Apart from variable accretion and/or obscuration, we briefly discuss a few other scenarios which could mimic changes in Seyfert type.

(i) Telescope offset: first, we note that apparent Seyfert-type changes could be caused by a slight mispointing of the Keck telescope, missing the AGN core and therefore the (bulk of the) broad emission lines. In all cases, the telescope was pointed at the center of the galaxy (as verified by guide star images), assuming that the AGN resides there. For a couple of extreme objects, the AGN might actually be offset from the center, as evidenced by the SDSS images; we discuss them below. Note that for all objects for which the AGN core and BLR coincide with the center of the galaxy, the possibility of missing the BLR emission due to a telescope offset is negligible, given the seeing ($\sim 1''$ for the Keck observations) and the slit width used ($1''$, matching the typical seeing), as verified by standard-star observations. Keck telescope guiding is also much more accurate than $1''$.

(ii) Galaxy mergers and/or recoiling SMBH: in the course of ongoing galaxy mergers, the AGN can appear offset from the apparent center of the merging system. It is therefore possible that an off-center AGN was captured by the wider, circular SDSS aperture, but missed during subsequent observation by the narrower Keck slit that was aligned along the major axis of the galaxy and centered on the galactic nucleus. Alternatively, a rare gravitational wave recoil following the final coalescence of two SMBHs in a merger can remove the newly formed single SMBH from the center of its host galaxy (e.g., see the review by Sperhake 2015). The accretion disk and BLR would remain bound and a recoiling SMBH would therefore appear as an AGN offset from the core of its host galaxy (Komossa 2012), again leading to the possibility of missing the (bulk of the) BLR in the narrower (and rectangular) Keck slit.

With the exception of a few cases (4/102, see Bennert et al. 2015); there are no signs for merger activity in the sample. However, we caution that merger signatures such as faint tidal tails might easily be missed in the low S/N SDSS images. Objects 0847+1824 and 1038+4658 show extended emission in the SDSS multi-color images, offset from the galaxy center (Figure 11), which might indicate the presence of an ongoing merger. While we cannot exclude the possibility that these are off-center AGNs, it is statistically unlikely to have off-centered AGNs in such a small sample, and follow-up spectroscopy would be needed to test such a scenario further. We note in passing that 0847+1824 seems to show a small kinematic offset between its narrow and broad Hβ line (with the broad Hβ line being blueshifted by ~ 100 km s^{-1}), which is, however, most likely mimicked by the asymmetric broad-line profile.

(iii) Supernovae: a SN IIn has many of the same spectral features as a Seyfert galaxy (Filippenko 1997). A nuclear supernova could have therefore mimicked the presence of an AGN. However, supernova spectra including the narrow emission lines evolve rapidly, and we do not see any other signs of dramatic changes in the continuum and narrow emission lines.

(iv) Stellar tidal disruption event: stars can be tidally disrupted and accreted by SMBHs, producing a luminous accretion flare (e.g., Rees 1988). If these occur in a gas-rich environment, broad and narrow emission lines can be temporarily excited. While a few candidate events for this process have been identified recently from SDSS (e.g., Komossa et al. 2008), these events are rare and unlikely to occur in our small sample. In particular, we have checked the long-term Catalina lightcurves of all three sources and none show the characteristic lightcurve decline expected for a typical tidal disruption event.

We are left with mild changes in accretion or extinction as the most likely explanation for the three changing look AGN in our sample. Future spectroscopic monitoring of emission line and continuum changes will enable us to distinguish between both possibilities. (Note that a difference in aperture between Keck and SDSS cannot explain the extreme Seyfert-type changes we observe in these three objects since it would have the opposite effect.)

4.4. Comparison with the Catalina Sky Survey

To further shed light on the causes for the observed variability, we considered the optical lightcurves in the Catalina Sky Survey (CSS) (Drake et al. 2009). With the exception of 1104+4334 and 1206+4244, all objects in our sample are in the CSS archive. (Note that 1605+3305 is in the archive, but it does not have a lightcurve available.) For most objects, CSS lightcurves begin after the SDSS observations, but extend past the time of the Keck and Lick observations; the lightcurves start and end at approximately $\sim 53500 - 56500$ MJD (~ 3000 days). The lightcurves of seven objects (0310−0049, 0904+5536, 1147+0902, 1355+3834, 1434+4839, 1535 +5754, and 1557+0830)[9] reveal large variability ($\sim 0.5 - 1$ mag in one object) over timescales from days to months to years. None of these objects are among our extreme subset of objects (see Table 2 for Seyfert types).

---

[9] Note that 0301+0110 shows a highly variable lightcurve, but upon further inspection it becomes clear that that is an artifact of a nearby bright star.

Since CSS photometry is aperture-based (Drake et al. 2009), we cannot exclude that a variable seeing can mimic variability since more or less of the host galaxy would be included in an aperture centered on the AGN. However, especially the extreme variability in these seven objects is unlikely to be purely a seeing effect. Independent analysis, which is beyond the scope of this paper, is needed to further confirm the observed variability.

5. SUMMARY

In this paper, we study the broad Hβ emission line variability in a sample of 102 local Seyfert 1 galaxies, selected from SDSS and re-observed three to nine (on average 6.4 ± 1.8) years later with LRIS on the 10 m Keck-I telescope.

In the three to nine year time frame between observations, 67/102 ($\sim$66%) objects show at least some form of variability of either width and/or strength of the broad Hβ line. For 39/102 ($\sim$38%) objects, this variability is significant enough to result in a change in Seyfert type, following the standard Seyfert classification scheme. There is no correlation between the time between observations and the degree of the observed Seyfert-type transition, implying that the transitions happen on shorter timescales. Short-time variability on the scale of days and weeks is known for low-mass AGNs from reverberation mapping. Almost all objects (99/102) were observed as part of the CSS with 7/102 ($\sim$7%) displaying significant variability on timescales of days to weeks.

Three ($\sim$3%) objects are extreme cases for which the broad Hβ component almost completely disappears. We discuss possible origins for these transitions. For two of these objects (0847+1824 and 1038+4658), SDSS images reveal extended emission off-centered from the galaxy center which could have been included in the SDSS spectra, but missed by the smaller-area Keck slit centered on the galaxy.

The study presented here is the first to provide statistical information on the frequency and strength of Hβ line variability in a sample of low-redshift Seyfert galaxies.

REFERENCES

Adelman-McCarthy, J. K., Agueros, M. A., Allam, S. S., et al. 2008, ApJ, 175, 297
Antonucci, R. R. J., & Cohen, R. D. 1983, ApJ, 271, 564
Arcavi, I., Gal-Yam, A., Sullivan, M., et al. 2014, ApJ, 793, 38
Aretxaga, I., Joguet, B., Kunth, D., Melnick, J, & Terlevich, R. J. 1999, ApJL, 519, L123
Barth, A. J., Bennert, V. N., Canalizo, G., et al. 2015, ApJS, 217, 26
Bennert, V. N., Auger, M. W., Treu, T., Woo, J. H., & Malkan, M. A. 2011, ApJ, 726, 59
Bennert, V. N., Treu, T., Auger, M. W., et al. 2015, ApJ, 809, 20
Bentz, M. C., Denney, K. D., Cackett, E. M., et al. 2007, ApJ, 662, 205
Bentz, M. C., Denney, K. D., Grier, C. J., et al. 2013, ApJ, 767, 149
Bochkarev, N. G. 2006, ASPC, 360, 285
Boroson, T. A., & Green, R. F. 1992, ApJS, 80, 109
Denney, K. D., Peterson, B. M., Dietrich, M., Vestergaard, M., & Bentz, M. C. 2009, ApJ, 692, 246
Denney, K. D., Rosa, G. D., Croxall, K., et al. 2014, ApJ, 796, 134
Dimitrijević, M. S., Popović, L. Č., Kovačević, J., Dačić, M., & Ilić, D. 2007, MNRAS, 374, 1181
Drake, A. J., Djorgovski, S. G., Mahabal, A., et al. 2009, ApJ, 696, 870
Elitzur, M., Ho, L. C., & Trump, J. R. 2014, MNRAS, 438, 3340
Eracleous, M., & Halpern, J. P. 2001, ApJ, 554, 240
Ferrarese, L., & Merrit, D. 2000, ApJL, 539, L9
Filippenko, A. V. 1997, ARA&A, 35, 309
Gebhardt, K., Bender, R., Bower, G., et al. 2000, ApJL, 539, L13
Goad, M. R., & Korista, K. T. 2014, MNRAS, 444, 43
Goodrich, R. W. 1989, ApJ, 340, 190
Graham, A. 2016, in Galactic Bulges, ed. E. Laurikainen, R. F. Peletier, & D. A. Gadotti, Vol. 418 (Berlin: Springer), 263
Harris, C. E., Bennert, V. N., Auger, M. W., et al. 2012, ApJS, 201, 29
Hicks, E. K. S., & Malkan, M. A. 2008, ApJS, 174, 31
Ho, L. C., & Kim, M. 2009, ApJS, 184, 398
Kaspi, S., Maoz, D., Netzer, H., et al. 2005, ApJ, 629, 61
Kollatschny, W., & Fricke, K. J. 1985, A&A, 146, L11
Komossa, S. 2012, AdAst, 2012, 364973
Komossa, S., Zhou, H., Wang, T., et al. 2008, ApJL, 678, L13
Korista, K. T., & Goad, M. R. 2004, ApJ, 606, 749
Kormendy, J., & Ho, L. C. 2013, ARAA, 51, 511
Kormendy, J., & Richstone, D. 1995, ARA&A, 33, 581
Kovacevic, J., Popovic, L. C., & Dimitrijevic, M. S. 2010, ApJS, 189, 15
LaMassa, S. M., Cales, S., Moran, E. C., et al. 2015, ApJ, 800, 144
Leighly, K. M., Cooper, E., Grupe, D., et al. 2015, ApJL, 809, L13
Lyutyi, V. M., Oknyanskii, V. L., & Chuvaev, K. K. 1984, SvAL, 10, 335
MacLeod, C. L., Ross, N. P., Lawrence, A., et al. 2016, MNRAS, 457, 389
Magorrian, J., Tremaine, S., Richstone, D., et al. 1998, AJ, 115, 2285
McGill, K. L., Woo, J. H., Treu, T., & Malkan, M. A. 2008, ApJ, 673, 703
Merloni, A., Dwelly, T., Salvato, M., et al. 2015, MNRAS, 452, 69

Nicastro, F. 2000, ApJL, 530, L65
Osterbrock, D. E. 1977, ApJ, 215, 733
Osterbrock, D. E. 1981, ApJ, 249, 462
Osterbrock, D. E. 1989, Astrophysics of Gaseous Nebulae and Active Galactic Nuclei (Mill Valley, CA: Univ. Science Books)
Osterbrock, D. E., & Koski, A. T. 1976, MNRAS, 176, 61
Pancoast, A., Brewer, B. J., Treu, T., et al. 2014, MNRAS, 445, 3073
Park, D., Woo, J. H., Bennert, V. N., et al. 2015, ApJ, 799, 164
Park, D., Woo, J. H., Treu, T., et al. 2012, ApJ, 747, 30
Parker, M. L., Fabian, A. C., Matt, G., et al. 2015, MNRAS, 447, 72
Penston, M. V., & Perez, E. 1984, MNRAS, 211, 33
Peterson, B., Denney, K. D., De Rosa, G., et al. 2013, ApJ, 779, 109
Rees, M. J. 1988, Natur, 333, 523
Rosenblatt, E. I., Malkan, M. A., Sargent, W. L. W., & Readhead, A. C. S. 1994, ApJS, 93, 73
Ruan, J. J., Anderson, S. F., Cales, S. L., et al. 2015, ApJ, submitted (arXiv:1509.03634)
Runnoe, J. C., Cales, S., Ruan, J. F., et al. 2016, MNRAS, 455, 1691

Scott, B. 2013, Time Variation of the Broad Hβ and Hα Emission Lines in Active Galactic Nuclei, Cal Poly Digital Commons
Shapovalova, A. I., Popovic, L. C., Burenkov, A. N., et al. 2010, A&A, 509, A106
Shappee, B. J., Prieto, J. L., Grupe, D., et al. 2014, ApJ, 788, 48
Shen, J., Vanden Berk, D. E., Schneider, D. P., & Hall, P. B. 2008, ApJ, 135, 928
Shen, Y., Richards, G. T., Strauss, M. A., et al. 2011, ApJS, 194, 45
Sperhake, U. 2015, ASSP, 40, 185
Storchi-Bergmann, T., Baldwin, J. A., & Wilson, A. S. 1993, ApJL, 410, L11
Tohline, J. E., & Osterbrock, D. E. 1976, ApJL, 210, L117
Trippe, M. L., Crenshaw, D. M., Deo, R., & Dietrich, M. 2008, AJ, 135, 2048
Valdez, F., Gupta, R., Rose, J. A., Singh, H. P., & Bell, D. J. 2004, ApJS, 152, 251
van der Marel, R. P., Cretton, N., de Zeeuw, P. T., & Rix, H. 1998, ApJ, 493, 613
van der Marel, R. P., & Franx, M. 1993, ApJ, 407, 525
Wandel, A., Peterson, B. M., & Malkan, M. A. 1999, ApJ, 526, 579
Woo, J. H., Treu, T., Malkan, M. A., & Blanford, R. D. 2006, ApJ, 645, 900